JGR Atmospheres

RESEARCH ARTICLE
10.1029/2024JD041576

How Porosity Influences the Heterogeneous Ice Nucleation Ability of Secondary Organic Aerosol Particles

Robert Wagner[1], Yaqiong Hu[1], Pia Bogert[1], Kristina Höhler[1], Alexei Kiselev[1], Ottmar Möhler[1], Harald Saathoff[1], Nsikanabasi Umo[1], and Marco Zanatta[1,2]

[1]Institute of Meteorology and Climate Research, Karlsruhe Institute of Technology, Karlsruhe, Germany, [2]Now at National Research Council, Institute of Atmospheric Sciences and Climate, Bologna, Italy

Key Points:

- Regardless of particle morphology, pure secondary organic aerosol particles are inefficient at nucleating ice under cirrus conditions
- A pristine coating layer of secondary organic matter deactivates efficient ice nucleating particles such as mineral dust and coal fly ash
- Ice cloud-processing changes the structure of the coating layer and partially restores the ice nucleation ability of such mixed particles

Correspondence to:
R. Wagner,
Robert.Wagner2@kit.edu

Citation:
Wagner, R., Hu, Y., Bogert, P., Höhler, K., Kiselev, A., Möhler, O., et al. (2024). How porosity influences the heterogeneous ice nucleation ability of secondary organic aerosol particles. *Journal of Geophysical Research: Atmospheres*, *129*, e2024JD041576. https://doi.org/10.1029/2024JD041576

Received 15 MAY 2024
Accepted 4 OCT 2024

Author Contributions:
Conceptualization: Robert Wagner
Formal analysis: Robert Wagner, Yaqiong Hu, Pia Bogert, Alexei Kiselev, Marco Zanatta
Funding acquisition: Ottmar Möhler, Marco Zanatta
Investigation: Robert Wagner, Yaqiong Hu, Pia Bogert, Alexei Kiselev, Harald Saathoff, Marco Zanatta
Resources: Nsikanabasi Umo
Supervision: Robert Wagner, Kristina Höhler
Visualization: Robert Wagner, Alexei Kiselev
Writing – original draft: Robert Wagner
Writing – review & editing: Robert Wagner, Yaqiong Hu, Pia Bogert, Kristina Höhler, Alexei Kiselev, Ottmar Möhler, Harald Saathoff, Nsikanabasi Umo, Marco Zanatta

Abstract During processing in deep convective cloud systems, highly viscous or glassy secondary organic aerosol (SOA) particles can develop a porous structure through a process known as atmospheric freeze-drying. This structural modification may enhance their heterogeneous ice nucleation ability under cirrus conditions through the pore condensation and freezing mechanism. Pristine, compact SOA particles, on the other hand, are recommended to be treated as ice-inactive in models. This recommendation also applies to internally mixed particles, where a coating layer of secondary organic matter (SOM) deactivates the intrinsic ice nucleation ability of the core, which may be a mineral dust grain. Ice cloud-processing may also improve the ice nucleation ability of such a composite particle by inducing structural changes in the coating layer, which can release active sites on the mineral surface. In this work, we investigated the change in the ice nucleation ability of pure SOA particles from the ozonolysis of α-pinene and two types of internally mixed particles (zeolite and coal fly ash particles coated with SOM) after being subjected to the atmospheric freeze-drying process simulated in an expansion cloud chamber. For pure α-pinene SOA, we found only a slight improvement in the ice nucleation ability of the ice cloud-processed, porous particles compared to their pristine, compact counterparts at 221 and 217 K. In contrast, the zeolite and coal fly ash particles, which were initially deactivated by the organic coating, became significantly more ice-active after atmospheric freeze-drying, emphasizing that such composite particles cannot be excluded from model simulations of heterogeneous ice formation.

Plain Language Summary Understanding how ice crystals form in the Earth's atmosphere is important for predicting climate using cloud models. It is believed that certain surface features on atmospheric aerosol particles, such as cracks and pores found on mineral dust grains, can effectively induce ice formation. Ice crystals are formed from small amounts of liquid water that have condensed and frozen in the pores of the particles. As a result, ice formation is less likely to occur on solid particles that lack such pores and have a smooth surface. One type of the latter are particles formed by the condensation of volatile, biogenic and anthropogenic organic compounds. In models of ice formation, such secondary organic aerosol particles are often neglected because of their compact, non-porous shape. In our work, we simulated a pathway by which such particles can acquire a porous structure through cloud-processing in the atmosphere, and investigated how this affects their ability to form ice. We also investigated mixed particle types in which the organic compounds condensed on a mineral surface, blocking the pores that allowed efficient ice formation. The aforementioned cloud-processing partially restructured the organic material on the mineral surface, and the particles became more effective at forming ice again.

1. Introduction

The pore condensation and freezing (PCF) mechanism provides an alternative view of heterogeneous ice formation on solid aerosol particles, so-called ice-nucleating particles (INPs), under cirrus conditions (Christenson, 2013; David et al., 2019; Fukuta, 1966; Kovács & Christenson, 2012; Marcolli, 2014). In the classical view, ice nucleation is described by the deposition nucleation mode, where ice is formed directly from the supersaturated vapor phase, that is, in an environment where the ice saturation ratio, S_{ice}, exceeds unity (Vali et al., 2015). The PCF mechanism consists of two distinct steps. The first step requires the presence of suitable cracks, capillaries, or pores on the particle surface that allow condensation of liquid, supercooled water at a relative humidity (RH_{liq}) below water saturation due to the inverse Kelvin effect. In the second step, the homogeneous freezing of supercooled water in the pores at $T \leq 235$ K and the growth of ice out of the pores at $S_{ice} > 1$ then lead to the formation of macroscopic ice crystals.

The PCF mechanism has attracted renewed interest due to the impetus by Marcolli (2014), as it provides a valid explanation for the sudden increase in the heterogeneous ice nucleation ability of a variety of aerosol particles once the temperature drops below the threshold for homogeneous freezing of pore water at about 235 K. In contrast, such a pronounced discontinuity in the ice nucleation behavior cannot be explained by the deposition nucleation mode (Marcolli, 2014). The involvement of the PCF pathway in heterogeneous ice formation has been strongly supported by recent experimental results. A compelling example was presented by David et al. (2019), where otherwise chemically identical silica particles were synthesized with either mesopores or non-porous and showed a significant difference in their ice nucleation behavior at 223 K (Figure 2a therein). In another case, Campbell and Christenson (2018) investigated ice nucleation in wedge-shaped cavities between two mica layers, called mica pockets. In accordance with the two-step PCF concept, they first observed ice growth within the pockets before bulk ice crystals emerged from the pocket corners. As a final example, experiments at the Aerosol Interaction and Dynamics in the Atmosphere (AIDA) cloud chamber have demonstrated pre-activation of certain types of aerosol particles (clay mineral illite and highly porous materials such as zeolite, diatomaceous earth, and coal fly ash) without prior macroscopic ice growth, simply by cooling the particles temporarily to temperatures below 228 K, where ice-filled pores can form due to PCF (Umo et al., 2019; Wagner et al., 2016). The latter pre-activation experiments are reminiscent of the work of Higuchi and Fukuta (1966) more than half a century ago, which, together with the study of Fukuta (1966), can be considered historically as the origin of the PCF concept. The more recent studies have extended the theoretical basis and have also shown that the size and geometry of the pore, the wettability of the material, and a possible free energy barrier associated with ice growth out of a pore of a given geometry are all factors that ultimately determine at what S_{ice} onset the actual formation of bulk ice crystals can be observed in experiments (Campbell & Christenson, 2018; David et al., 2019, 2020; Marcolli, 2020).

There are many atmospherically relevant aerosol particles that inherently have potentially PCF-active sites on their surface. These include mineral dust grains, where the active sites are found or are exposed in surface irregularities such as steps, cracks and cavities, or in voids created by the overlapping of crystal layers (Kiselev et al., 2017; Marcolli, 2014; Pach & Verdaguer, 2019; Wang et al., 2016). In the case of combustion soot, aggregation leads to cavities within the same or two adjacent layers of primary particles, which can initiate PCF (Mahrt et al., 2018, 2020; Marcolli et al., 2021). As another example, electron microscope images of coal fly ash particles reveal very irregularly shaped surfaces with deposits of mesh-like and spongy material with high porosity (Umo et al., 2019). Apart from these cases, there is one class of particles that can acquire a porous structure through atmospheric cloud-processing, namely highly viscous, secondary organic aerosol (SOA) particles.

SOA particles are formed in the atmosphere when the oxidation products of volatile, biogenic and anthropogenic organic compounds condense into the particulate phase (Hallquist et al., 2009). Their particle viscosity is highly variable, and at low temperatures and/or low humidity they may exist as highly viscous semi-solids or amorphous glassy solids (Koop et al., 2011; Reid et al., 2018; Virtanen et al., 2010). This is the key to understanding why such SOA particles can develop a highly porous structure when they are released in the outflow of a deep convective cloud system (Adler et al., 2013). In such cloud-processing, SOA particles with an initially compact shape are first activated to cloud droplets at warm temperatures, which then freeze homogeneously at a temperature $\leq$235 K. As the droplets freeze, an organic-rich solution phase separates from the ice, concentrates upon further ice growth, and eventually vitrifies. When ice sublimates at $S_{ice} < 1$ in the outflow of deep convection, highly porous SOA particles are left behind, whose cavities in the structure are exactly where the ice once was. This so-called atmospheric freeze-drying process was simulated in two laboratory setups, firstly with an aerosol flow system (Adler et al., 2013) and secondly with the AIDA cloud chamber (Wagner et al., 2017).

In addition to a previously demonstrated significant change in the optical properties (Adler et al., 2014; Haspel & Adler, 2017), the transition from a compact to a porous structure could have a critical impact on the ice nucleation ability of the SOA particles under cirrus conditions. Most ice nucleation measurements with pristine, compact SOA particles show ice formation starting at or above the homogeneous freezing conditions for aqueous solution droplets (Charnawskas et al., 2017; Kasparoglu et al., 2022; Ladino et al., 2014; Möhler et al., 2008; Piedehierro et al., 2021; Schill et al., 2014; Wagner et al., 2017). This indicates either that the particles liquefy completely, or at least in their outer layers, and exhibit a true homogeneous freezing mode, or that they remain semi-solid or glassy, but that ice formation in the deposition nucleation mode on the smooth, non-porous particle surface is inefficient and only occurs at high S_{ice} values. This observation can be extended to cases where other types of INPs, such as mineral dust or crystalline ammonium sulfate, are completely coated by a layer of secondary

organic matter (SOM) (Bertozzi, 2021; Bertozzi et al., 2021; Koehler et al., 2010). Heterogeneous ice formation was only observed in a few studies, for example, for naphthalene- and α-pinene-derived SOA at onset conditions slightly below the homogeneous freezing threshold (Ignatius et al., 2016; Wang et al., 2012), and with a very low ice-active fraction for isoprene-derived SOA (Wolf et al., 2020). Kasparoglu et al. (2022) therefore recently recommended treating glassy or liquid SOM and dust coated with glassy or liquid SOM as inefficient for heterogeneous ice formation in models. However, whether and how the porosity of the SOM material affects this recommendation is an important unanswered question that we aim to address in this study.

In principle, the transition from a smooth to a porous structure due to atmospheric freeze-drying could increase the capacity for heterogeneous ice nucleation, provided that the porous structure remains stable and does not collapse when the freeze-dried SOA particles released in the outflow of deep convection re-enter a region with $S_{ice} > 1$. However, as mentioned above, hydrophilicity, pore size and geometry are critical to the efficiency of the PCF mechanism. PCF of soot aggregates has been successfully modeled by applying different packing arrangements of primary particles and calculating capillary condensation in and ice growth from the resulting pores (Marcolli et al., 2021). The porous network of SOA particles is formed by the dynamic freeze-drying process and depends on the morphology of the temporarily formed ice crystal and the way in which the phase-separated, organic-rich phase is redistributed on it. As can be seen in the electron microscope images from the laboratory studies (Adler et al., 2013; Wagner et al., 2017), the porous SOA particles therefore have a very irregular structure, the theoretical description of which is far less certain than for soot. We therefore take a purely experimental approach to answering the above question. The existing experimental database on ice formation by cloud-processed, potentially porous organic particles is relatively sparse. There have been reports of cloud processing increasing the ice nucleation ability of the particles, but these were experiments with pure organic substances such as raffinose and levoglucosan (Kilchhofer et al., 2021; Wagner et al., 2012). Such organic proxies behave differently from complex SOM, as they frequently exhibit a heterogeneous freezing mode even for pristine, compact particles (Baustian et al., 2013; Ladino et al., 2014; Murray et al., 2010; Wilson et al., 2012). This can be due to deposition ice nucleation on the glassy particle surface or immersion freezing in a partially deliquesced particle with a glassy core and a liquefied outer layer (Berkemeier et al., 2014). To our knowledge, the only measurements of ice nucleation with porous SOA particles under cirrus conditions are our previous atmospheric freeze-drying experiments with α-pinene-derived SOA performed in the AIDA cloud chamber (Wagner et al., 2017).

In this previous study, the SOA particles were first cloud processed in expansion cooling experiments started at 243 K (Wagner et al., 2017). The activation of the organic aerosol particles into cloud droplets, followed by homogeneous freezing and sublimation of the ice crystals, left behind a population of porous particles, as revealed by electron microscope images (Wagner et al., 2017). The porous SOA particles were then cooled to 223 K over a period of 6 hr and their ice nucleation behavior was investigated in a further expansion cooling run and compared to reference experiments carried out beforehand with unprocessed, compact SOA particles at the same temperature. Compared to the unprocessed, compact SOA particles, the ice nucleation onsets of the porous particles showed only a very small decrease of about 0.05 on the S_{ice} scale, which is similar to the overall measurement uncertainty for S_{ice} (see Figure 8 in Wagner et al., 2017). However, the small number of only two experiments performed and experimental limitations related to possible restructuring of the SOA particles during the long cooling time to 223 K and larger temperature inhomogeneities in the cloud chamber due to the strong cooling prevented us from drawing definite conclusions.

In this article, we present an improved experimental procedure that allowed us to obtain a more comprehensive and robust data set on the heterogeneous ice nucleation capability of porous SOA particles. In this new approach, the AIDA chamber was used only as a reservoir to stabilize the porous SOA particles generated during the initial expansion cooling run at 243 K, while the actual ice nucleation measurements under cirrus conditions were performed with continuous flow diffusion chambers (CFDCs) sampling the particles from the chamber via a cooled sampling line. In a first set of experiments, we applied this procedure to pure SOA particles from the ozonolysis of α-pinene. Then we conducted atmospheric freeze-drying experiments with internally mixed particles. To this end, we condensed SOM from the ozonolysis of α-pinene onto two particle types that are inherently very efficient INPs under cirrus conditions, namely zeolite and coal fly ash (CFA) particles. In agreement with Kasparoglu et al. (2022), these INPs lost their heterogeneous ice nucleation ability after coating and could therefore be considered ice-inactive in models at first glance. However, we then simulated atmospheric freeze-drying of such a composite particle with the idea that this process could transform the organic coating layer from a compact to a porous structure, which in turn would re-expose active sites on the surface of the INP, thereby

restoring some of its intrinsic heterogeneous ice nucleation ability. Alternatively, the porous organic coating itself could open a path for heterogeneous ice formation via the PCF mechanism. An indication of such reactivation of organic-coated INPs during ice cloud processing was found in experiments with internally mixed particles of ammonium sulfate and SOM (Bertozzi et al., 2021).

Our article is organized as follows: Section 2 describes the basic instrumentation of the AIDA chamber, the particle generation methods, and the operation of the CFDCs for the ice nucleation measurements. The improved procedure for the atmospheric freeze-drying experiments is outlined in Section 3. The effect of freeze-drying on ice nucleation is then described in Section 4.1 for pure SOA particles and in Section 4.2 for internally mixed zeolite/SOM particles and CFA/SOM particles. Section 5 concludes the article with a summary.

2. Methods

2.1. General Setup and Instrumentation of the AIDA Aerosol and Cloud Chamber Facility

The general setup is very similar to the experiments presented in Wagner et al. (2017). We give a brief summary and conclude this section by presenting two additional characterization techniques employed in the present work, namely measurements of the effective density of the aerosol particles and ice nucleation measurements with the CFDCs. The aerosol and cloud chamber facility consists of two aerosol vessels, the 84 m^3 AIDA chamber and the 4 m^3 aerosol preparation and characterization chamber (APC) (Figure 1). We used AIDA for expansion cooling experiments to simulate atmospheric freeze-drying in ice clouds and to stabilize the resulting porous, organic-containing aerosol particles for a few hours for further characterization. The APC was used to produce SOA particles and SOM-coated zeolite and CFA particles in a controlled and reproducible manner before transferring them to the AIDA chamber for the atmospheric freeze-drying experiments. As described in Section 3, it also served as additional expansion volume during these AIDA expansion cooling runs.

The APC was operated at room temperature and was equipped with standard instrumentation for measuring the number concentration and size of the aerosol particles, including a condensation particle counter (CPC, model 3022, TSI), a scanning mobility particle sizer (SMPS, model 3071, TSI), and an aerodynamic particle spectrometer (APS, model 3321, TSI). For cleaning purposes, the chamber was evacuated to <1 hPa and filled to ambient pressure with dry, particle-free synthetic air with a frost point ≤200 K. The AIDA chamber is located in a cold box that allows temperature control between 333 and 183 K. The AIDA gas temperature reported below is the average of four thermocouples mounted at different heights inside the chamber, and was controlled to 243 K for the start of the atmospheric freeze-drying experiments. As explained in Section 3, it was necessary to prepare the AIDA chamber for these experiments under well-defined humidity conditions ($S_{ice} = 0.96$, corresponding to 72% RH_{liq} at 243 K). The procedure required for humidification is described in detail in Section 2.2. As with the APC, a similar suite of CPC, SMPS, and APS instruments was available at the AIDA chamber for the counting and sizing of aerosol particles. Aerosol particles with sizes larger than about 0.5 µm also extended into the measurement range of an optical particle counter (OPC1, type welas 2300, Palas GmbH), which counted and sized cloud droplets and ice crystals formed during the atmospheric freeze-drying experiments with 100% efficiency. For this purpose, the measurement cell of the OPC1 was mounted inside the isolating containment in the free space between the bottom of the aerosol vessel and the ground of the cold box (Figure 1).

The partial pressure of water vapor was measured in situ in the AIDA chamber with tunable diode laser (TDL) absorption spectroscopy (Fahey et al., 2014). The ratio of this vapor pressure to the saturation water vapor pressure over ice and liquid water at the given AIDA temperature yielded the saturation ratios S_{ice} and S_{liq} (Murphy & Koop, 2005), with RH_{liq} indicating S_{liq} as a percentage. The instrument SIMONE (Scattering Intensity Measurements for the Optical detectioN of icE) detected laser light of 488 nm wavelength scattered by aerosol and cloud particles in the center of the cloud chamber at two scattering angles, 2° and 178° (Schnaiter et al., 2012). Its measurement data are presented here in the form of the forward-to-backward scattering ratio σ, which corresponds to the ratio of the scattering intensity detected at 2° to that detected at 178°, where the latter was calculated from the sum of two polarization components (Schnaiter et al., 2012). An ESEM (Environmental Scanning Electron Microscope, type Quattro S, FEI, Thermo Fisher Scientific Inc.) was used for the morphological characterization of the particles before and after atmospheric freeze-drying. To preserve the porous structure, a vacuum cryo-transfer system (EM VCT500, Leica) was employed to ensure an uninterrupted chain of cryogenic transfer from particle sampling to electron microscopic analysis (Wagner et al., 2017, 2021). The central part of this unit was a liquid nitrogen-cooled transfer shuttle with a silicon sample substrate that could be

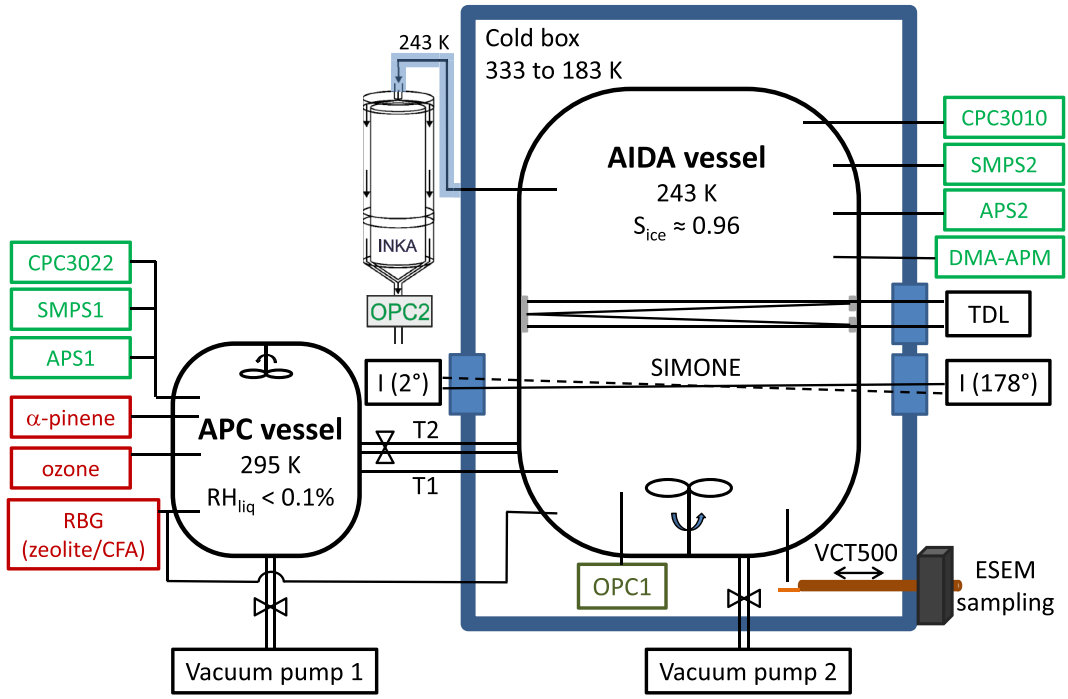

Figure 1. Schematic diagram of the aerosol and cloud chamber facility with the 84 m^3 AIDA vessel and the 4 m^3 APC vessel. Both chambers are continuously stirred by mixing fans installed above the bottom or under the top of the vessels. T1 is the 25 mm stainless steel connection tube mentioned in Section 2.2 for transferring aerosol particles from the APC to the AIDA chamber in type 1 through 3 experiments. T2 is a 100 mm connection tube between the two chambers used in the atmospheric freeze-drying experiments described in Section 3. The acronyms and operation of the scientific instruments for particle and trace gas generation and characterization are described in Sections 2.1 and 2.2.

moved into and out of the AIDA cold box through a pneumatic air lock. Particle deposition on the sampling substrate was electrostatically supported by connecting it to a high-voltage supply set to +2 kV and passing the aerosol flow from the AIDA chamber through a unipolar corona discharge device (CD, 2000 type A, Palas GmbH). The samples of cloud-processed SOM-coated CFA and CBV400 were observed under low vacuum conditions (at 50 Pa of nitrogen), whereas the pure SOA particles (unprocessed and processed by cloud activation and re-compaction, see Section 3) were sputter coated (ACE600, Leica) with 1.5 nm of Pt while maintaining the sample temperature at 173 K.

As another tool to document the transition from a compact to a porous structure, effective density measurements of the particles were performed using a tandem system consisting of a DMA (Differential Mobility Analyzer, model 3081, TSI) and an APM (Aerosol Particle Mass Analyzer, model 3601, Kanomax) (Rissler et al., 2013). The DMA was used for the size selection of particles sampled from the AIDA chamber through a diffusion dryer and was set to various mobility-equivalent diameters, d_{me}, between 200 and 500 nm. The mass distribution of the size-selected particles was then determined with the APM by increasing the rotational speed of the cylindrical electrodes during a 180-s scan period and measuring the particle number concentration downstream of the instrument with a CPC (model 3775, TSI) using a sample flow of 0.3 SLM. The median particle mass, m_p, was then derived by applying a Gaussian fit to the particle mass distribution obtained for each mobility diameter during such an APM scan. Finally, the effective density, ρ_{eff}, was obtained according to:

$$\rho_{\text{eff}} = \frac{6m_p}{\pi d_{me}^3} \quad (1)$$

Below, we report ρ_{eff} values calculated as the average of six individual measurements for d_{me} of 275, 300, 325, 350, 375, and 400 nm, where no size-dependent variations were apparent.

Table 1
Overview of the Types of Experiments Carried Out and the Methods of Particle Generation

Experiment type	Aerosol particle type	Particle generation method
1	SOA	Injection of 3.5 ppmv O_3 and 2.8 ppmv α-pinene into APC, reaction time 60 min, followed by particle transfer to AIDA (1,100–1,400 cm^{-3})
2	zeolite/SOM (+SOA)	Injection of 25,000 cm^{-3} zeolite particles into APC with RBG, addition of 1.7 ppmv O_3, addition of 15 ppbv min^{-1} α-pinene for 30 min, then particle transfer to AIDA (750 cm^{-3})
3	CFA/SOM (+SOA)	Injection of 26,000 cm^{-3} CFA particles into APC with RBG, addition of 1.5 ppmv O_3, addition of 15 ppbv min^{-1} α-pinene for 30 min, then particle transfer to AIDA (800 cm^{-3})
4	Zeolite	Direct injection into AIDA with RBG (800 cm^{-3})
5	CFA	Direct injection into AIDA with RBG (550 cm^{-3})

Note. As indicated by the brackets in the second column, a fraction of pure SOA particles was formed in addition to the SOM-coated zeolite and CFA particles in type 2 and type 3 experiments. Experiment type 1 was performed four times with slightly different numbers of particles transferred to the AIDA chamber in the range of 1,100–1,400 cm^{-3}. Experiments of types 2 to 5 were performed once.

Most ice nucleation measurements were carried out using a CFDC with a vertical cylindrical geometry called INKA (Ice Nucleation Chamber of the Karlsruhe Institute of Technology), a stationary instrument at the AIDA chamber that has been in operation since 2014 (Bertozzi, 2021; Bertozzi et al., 2024; Schiebel, 2017). Aerosol particles entering the CFDC were sampled from the AIDA chamber through a sampling tube cooled to 243 K to avoid potential restructuring of the porous particles during transient heating. Active cooling could not be applied in the short transition section with a residence time of less than a second, where the aerosol particles sampled from the AIDA chamber passed through a thin circular nozzle to reach the annular gap between the two temperature-controlled walls of the CFDC (Schiebel, 2017). However, this inlet section was well shielded with thermal insulation tape to minimize transient heating. In the applied humidity-scan mode, the temperature experienced by the aerosol particles was held constant while the humidity in the nucleation and growth section of the CFDC was gradually ramped from $S_{ice} = 1$ to $RH_{liq} = 100\%$ at a dS_{ice}/dt rate of approximately 0.03 min^{-1}. This was achieved by continuously decreasing the cold plate temperature and, at a slightly higher rate, increasing the warm plate temperature of the CFDC using pre-calculated temperature ramps controlled by two independent circulation chillers (Bertozzi, 2021; Schiebel, 2017). The position of the aerosol lamina as well as the ice saturation ratio and temperature at its center were calculated according to Rogers (1988), taking into account uncertainties in the measured wall temperatures of ±0.5 K and ±0.08 cm for the estimate of the gap width between the two ice-coated plates of the CFDC to obtain the error range for S_{ice} and T (Bertozzi et al., 2021; Schiebel, 2017). The result of a CFDC measurement at a given temperature was therefore an activity spectrum showing the ice-active fraction, f_{ice}, of the aerosol population as a function of S_{ice}. The ice-active fraction was calculated as the ratio of the number of nucleated ice crystals counted with the OPC2 (customized CI-3100, Climet, Figure 1) at the outlet of the CFDC to the number of the seed aerosol particles with an estimated uncertainty of ±30% (Wagner et al., 2020). Due to a malfunction of a cooler of the INKA instrument, its recently developed mobile version, called mINKA, was used instead in two experiments. Technical details of both CFDC types are given in Bertozzi (2021) and Bertozzi et al. (2024). The CFDC measurements were carried out in the temperature range between 233 and 217 K and are the central part of the discussion in Section 4.

2.2. Aerosol Types and Particle Generation

As summarized in Table 1, we conducted five different types of experiments using the following aerosol particles: (1) pure SOA particles from the ozonolysis of α-pinene, (2) zeolite particles coated with SOM from the ozonolysis of α-pinene, (3) CFA particles coated with SOM from the ozonolysis of α-pinene, (4) pure zeolite particles, and (5) pure CFA particles. For the first three types of experiments, we used the APC chamber for aerosol generation followed by particle transfer to the AIDA vessel, while the pure, uncoated zeolite and CFA particles were injected directly into the AIDA chamber.

Generation of pure, pristine SOA particles was initiated by the addition of approximately 3.5 ppmv ozone (Semozon 030.2 discharge generator, Sorbios) to the APC chamber, followed by the injection of 2.8 ppmv (1S)-(−)-α-pinene (99%, Aldrich). After a reaction time of about 1 hour, the nucleated SOA particles had grown to a median d_{me} of about 350 nm with a number concentration > 10^5 cm^{-3}. A portion of the APC chamber air was then

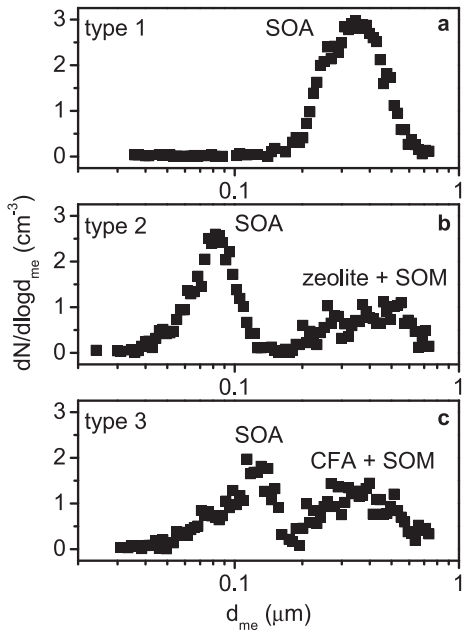

Figure 2. Normalized number size distributions measured with the SMPS after the aerosol particles were transferred from the APC to the AIDA chamber in experiments of type 1 (part a, pure SOA particles), type 2 (part b, SOM-coated zeolite particles), and type 3 (part c, SOM-coated CFA particles). As discussed in Section 2.2, nucleation modes of pure SOA particles were formed in addition to the SOM-coated particle modes in the type 2 and 3 experiments.

flushed through a 25 mm stainless steel connection tube into the AIDA chamber, which was maintained at 243 K. The transfer was initiated by setting a 30 SLM sample flow from the AIDA chamber, opening the APC-to-AIDA connection valve, and supplying a 30 SLM add flow of synthetic air to the APC for pressure balance. The AIDA air, which was initially free of particles, was thus partly replaced by the APC air, which was rich in SOA particles. The connection valve was closed when the particle number concentration in AIDA had reached 1,100–1,400 cm^{-3}. In total, we performed four freeze-drying experiments with pure SOA particles produced in this way. A representative size distribution measurement of the SOA particles after the transfer to the AIDA chamber is shown in Figure 2a. In our previous study (Wagner et al., 2017), we measured the composition of the SOA particles using a high-resolution time-of-flight aerosol mass spectrometer (HR-ToF-AMS, Aerodyne), which was not available for this work. Due to similar conditions for SOA particle formation in terms of temperature, RH_{liq}, and reaction time, we expect that the values derived from the earlier study, that is, mean oxygen-to-carbon (O/C) and hydrogen-to-carbon (H/C) ratios of 0.35 and 1.55, respectively, are also reasonable estimates for the particle composition in the current study.

As mentioned above and explained in more detail in Section 3, accurate control of the humidity in the AIDA chamber to S_{ice} = 0.96 at 243 K was critical for the successful simulation of the atmospheric freeze-drying process. Prior to transferring the particles from the APC to the AIDA chamber, the humidity in AIDA was set to $S_{ice} \approx 0.75$. This was achieved by evaporating an equivalent amount of water from a heated reservoir into the evacuated aerosol vessel held at 243 K and then refilling it with dry synthetic air to ambient pressure. The partial replacement of the humidified AIDA air with the dry air from the APC vessel during particle transfer resulted in a small decrease in S_{ice}. Before starting the atmospheric freeze-drying experiments, the AIDA air was further humidified to S_{ice} = 0.96 by injecting a flow of 15 SLM synthetic air passed over a water reservoir heated to 323 K. This controlled humidification procedure made it possible to establish a humidity close to ice-saturated conditions, but avoided the addition of excess water that could form a layer of ice on the inner walls of the AIDA chamber, which would have been unfavorable for the atmospheric-freeze drying experiment (Section 3).

Zeolite and CFA particles were produced from dry powders using a rotating brush generator (RBG, type RBG1000, Palas GmbH) adapted with two impactor stages of a cyclone system (d_{50} cutoff of 1.2 µm). The zeolite sample was a commercially available powder (trade name CBV400, Zeolyst International) synthesized to have an artificial mesoporous network with mesopores ranging in diameter from 4 to 20 nm (Janssen et al., 2002) and was used as is. The coal fly ash sample was obtained from one of the major power plants in the UK and sieved to obtain the 0–20 µm size fraction for particle generation with the RBG (Umo et al., 2019). These procedures followed our earlier experiments conducted with the two aerosol particle types, where we had investigated ice formation by the PCF mechanism (Umo et al., 2019; Wagner et al., 2016).

In the type 2 and 3 experiments (Table 1), the aim was to fully coat the zeolite and CFA particles with SOM from the ozonolysis of α-pinene to completely deactivate their intrinsic heterogeneous ice nucleation ability. This required the formation of a sufficient amount of condensable organics, while ensuring that these materials condensed to a significant degree on the pre-added zeolite and CFA particles, rather than nucleating pure SOA particles. The optimum settings were determined from a series of test experiments in the APC chamber and consisted of providing a very high seed aerosol particle number concentration (about 25,000 cm^{-3}), adding a moderately high concentration of ozone (1.5–1.7 ppmv), and injecting a small, continuous flow of α-pinene (about 15 ppbv min^{-1}) for a total reaction time of 30 min. After this period, the transfer of particles from the APC to the AIDA chamber was started as described above, until a number concentration of 750–800 cm^{-3} was reached in the large cloud chamber. Here, a higher purge flow of 300 SLM had to be used due to the lower overall particle number concentration in the APC vessel compared to the SOA-only experiments of type 1. As shown in the SMPS size distribution measurements in Figures 2b and 2c, nucleation of pure SOA particles could not be completely

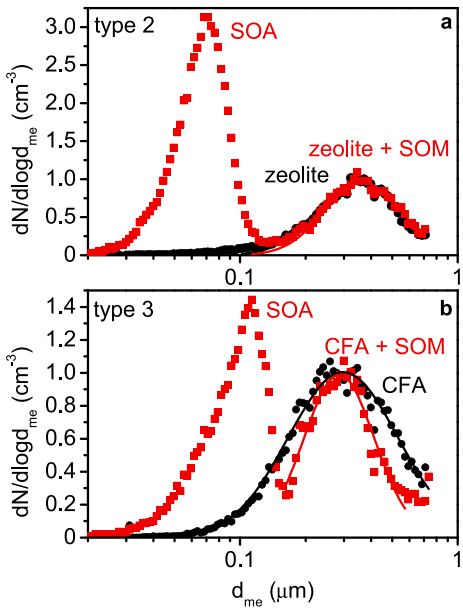

Figure 3. Normalized number size distributions measured with the SMPS in the APC chamber during particle generation in the type 2 (part a) and type 3 (part b) experiments. The black dots indicate the measurements of the pre-added, still uncoated zeolite and CFA particles. Black lines represent log-normal fits to the SMPS data points. The red squares show the size distribution measurements taken after 30 min of exposure to ozone and α-pinene, shortly before the particles were transferred to the AIDA chamber. They show two modes consisting of the SOM-coated zeolite and CFA particles and the newly nucleated pure SOA particles. Red lines represent log-normal fits to the SOM-coated particle modes. Since the number concentration of zeolite and CFA particles decreased during the coating period due to sedimentation losses, the red squares have been scaled to correspond to the peaks of the size spectra of the uncoated particles for better comparison. Slight differences between the size spectra measured at the end of the coating process in the APC chamber (red squares in parts a and b) and those measured after particle transfer in the AIDA chamber (Figure 2, parts b and c) can be explained by the relatively long transfer time of about 20 min, during which the coating process was still ongoing in the APC chamber.

avoided, so the coating process produced an externally mixed particle population. For type 2, the mixture consisted of about 62% (by number) pure SOA particles (median $d_{me} \approx 85$ nm) and 38% SOM-coated zeolite particles ($d_{me} \approx 400$ nm), while for type 3, new particle formation could be suppressed to a slightly greater extent yielding 50% pure SOA particles ($d_{me} \approx 120$ nm) and 50% SOM-coated CFA particles ($d_{me} \approx 350$ nm). The coating parameters in type 2 and 3 experiments were similar to those used in our previous study to coat 400 nm-sized crystalline ammonium sulfate particles with SOM from the ozonolysis of α-pinene in the APC chamber (Bertozzi et al., 2021). There, we obtained organic mass fractions in the range of 27%–47%, which we consider to be a reasonable estimate for the present experiments. As mentioned above, the HR-ToF-AMS was not available in the present study to directly measure the organic mass concentration.

In the case of zeolite particles coated with SOM, it makes sense to speak of a layer thickness of the organic material. As previously acquired ESEM images show, the bare CBV400 zeolite particles have a fairly compact habit (Wagner et al., 2016). The high degree of porosity due to the artificial network of small mesopores was visible by the high transparency of the particles to the electron beam. During the 30 min reaction time in the APC chamber, we observed a small increase in the mobility diameter of the particles of approximately 20 nm (Figure 3a). Therefore, it could be argued that the organic material formed a coating layer on the outer surface of the particles and was not only consumed to penetrate and fill the internal mesoporous network. For the SOM-coated CFA particles, we observed an even more significant change in the size distribution, but instead of a size shift, a pronounced reduction in the mode width was observed (Figure 3b). Since the overall shape of CFA particles is highly irregular and rich in larger cavities (Umo et al., 2019), we believe that the addition of organic material, rather than increasing the macroscopic particle dimension, resulted in the filling of these internal voids. This could be the explanation for the reduction in the width of the size distribution, as the coating process led to a population of more compact, homogeneously distributed particle shapes. Further discussion of particle morphology, including new ESEM images taken in this work, follows the analysis of the ice nucleation measurements with the SOM-coated zeolite and CFA particles in Section 4.2.

Type 4 and 5 experiments served as a reference to measure the ice nucleation ability of the uncoated zeolite and CFA particles with the CFDCs. We performed these reference measurements under exactly the same conditions as for the SOM-coated particles, that is, the particles were sampled from the AIDA chamber conditioned to 243 K and $S_{ice} = 0.96$. As the intermediate step of generating the particles in the APC vessel was unnecessary, they were injected directly into the AIDA chamber using the RBG. All experiments of types 2 to 5 were conducted once.

3. Atmospheric Freeze-Drying Simulated in the AIDA Chamber

With a controlled reduction in chamber pressure by a vacuum pump located in the basement of the facility (Figure 1), the humid air in the AIDA chamber can be expanded, causing it to cool and form a supersaturated vapor. Vapor condensation on the pre-added aerosol particles, followed by homogeneous freezing of the cloud droplets upon continued cooling to $T \leq 235$ K, are the key steps of the atmospheric freeze-drying process that can be simulated in such an expansion cooling experiment. Figure 4 illustrates the detailed procedure for a type 1 experiment with pure SOA particles using time series of different AIDA measurement data, organized in four parts: Part a: AIDA pressure (p, black line) and mean gas temperature (T, red line); part b: saturation ratios with respect to ice and supercooled liquid water (S_{ice}, brown line, and S_{liq}, magenta line); part c: optical diameters of aerosol particles and hydrometeors measured with the OPC1 (green dots), total particle count rate measured with the OPC1 (N_{OPC1}, blue line) and aerosol particle number concentration measured with the CPC (N_{CPC}, orange line); part d: forward-to-backward scattering ratio measured with the SIMONE instrument (σ, gray line).

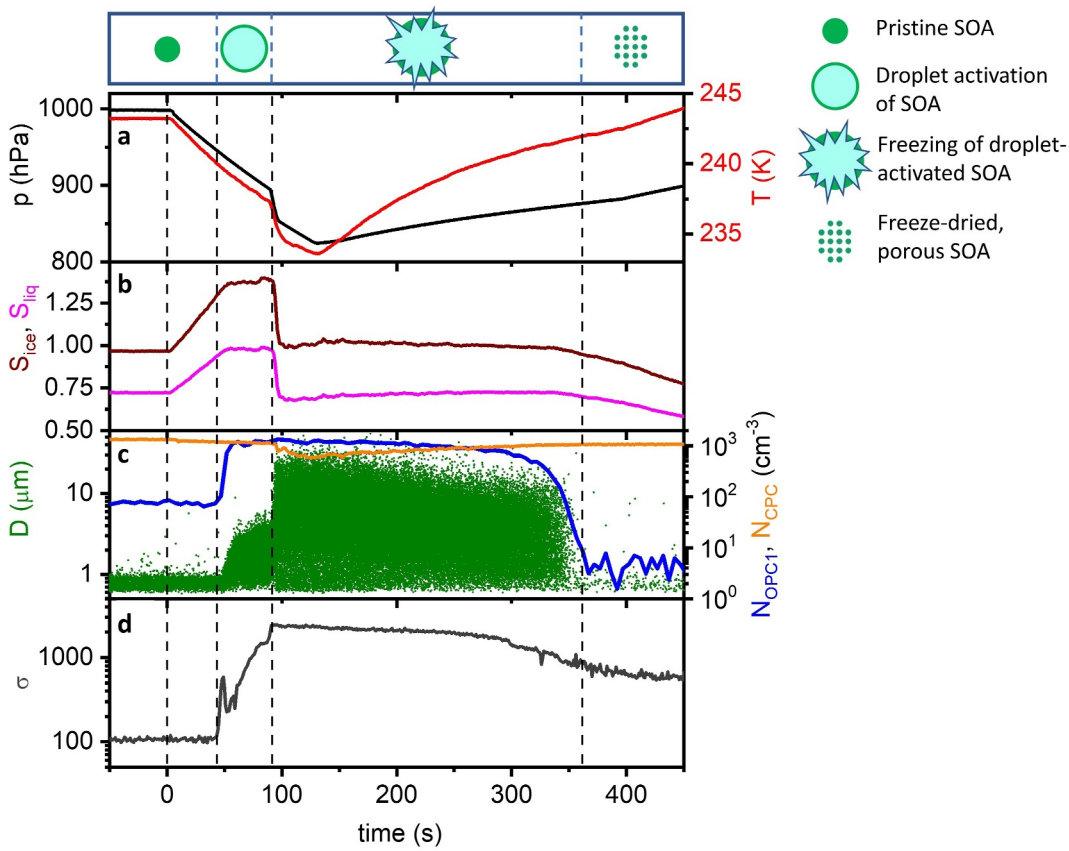

Figure 4. AIDA measurement data during an atmospheric freeze-drying experiment with pure SOA particles from the ozonolysis of α-pinene (type 1, Table 1). The processing of the particles during the experiment is symbolized by the pictograms at the top. The zero point of the time axis marks the start of pumping. Part (a) AIDA pressure (black) and mean gas temperature (red). (b) Saturation ratios with respect to ice (S_{ice}, brown) and supercooled liquid water (S_{liq}, magenta). (c) Optical diameters of SOA particles and hydrometeors detected by the OPC1 (green dots), total particle count rate measured by the OPC1 (N_{OPC1}, blue line), and particle number concentration measured with the CPC (N_{CPC}, orange line). (d) Forward-to-backward (2°-to-178°) scattering ratio measured by the SIMONE instrument (σ, gray line). To account for the gain difference between the photomultipliers for detecting forward and backward scattered light, σ was scaled to reproduce forward Mie calculations of the expected SIMONE scattering intensities during the period when the supercooled liquid cloud was present (Schnaiter et al., 2012).

The static temperature and humidity conditions of the experiment prior to the start of pumping at time zero were 243 K and 72% RH_{liq} (S_{ice} = 0.96). These conditions were carefully considered and are the result of several interacting factors that we want to explain briefly before describing the data in Figure 4. The main experimental limitation is that the walls of the AIDA chamber cannot be actively cooled during the expansion, so that their temperature remains nearly constant throughout the experiment. The increasing temperature difference between the chamber walls and the gas volume leads to an increasing heat flux into the volume and reduces the cooling rate, eventually preventing any further cooling of the volume, thus limiting the dynamic range of the experiments to a gas temperature decrease of about 10 K. Therefore, the starting temperature has to be low enough to reach the homogeneous freezing temperature of the supercooled cloud droplets in the later part of the expansion run. On the other hand, the starting temperature must still be high enough to allow prior droplet activation at $T > 235$ K and efficient mixing of the organic material in the liquid phase before homogeneous freezing of the cloud droplets occurs at $T \leq 235$ K. A starting temperature of 243 K was found to be an appropriate value to ensure that both of these conditions were met. The requirement for prior droplet activation also necessitates a high relative humidity at the start of expansion cooling to ensure that RH_{liq} exceeds 100% before the gas temperature has already dropped to 235 K. The chosen RH_{liq} = 72% is close to the maximum value of the relative humidity that can be achieved, which is limited by the saturation water vapor pressure over a surface of ice at 243 K.

Returning to Figure 4, we consider the OPC1 data in part c as the most illustrative measurement data for analyzing the progress of the atmospheric freeze-drying experiment. Before the start of expansion cooling (first vertical line), a small fraction of about 6% of the total number concentration of the pristine SOA particles extended into the measurement range of the OPC1 ($N_{OPC1} \approx 80$ cm^{-3}, $N_{CPC} \approx 1{,}300$ cm^{-3}). These particles reached optical diameters up to 1 μm in the OPC1 single-particle data. After cooling to 240 K (second vertical line), the air was supersaturated with respect to supercooled water, and the formation of super-micron-sized cloud droplets could be observed in the OPC1 records. Now, N_{OPC1} was almost equal to N_{CPC}, emphasizing that most SOA particles had been activated into cloud droplets. The growth of the cloud droplets initially caused some oscillations and then a steady increase of the forward-to-backward scattering ratio σ (part d). While the liquid cloud was present, RH_{liq} leveled off at 100% (part b).

After further cooling to 237 K (third vertical line), we induced a discontinuity in the expansion profile (part a). Instead of continuing with a constant pumping speed, we opened the connection valve to the now evacuated APC chamber to induce a rapid super-expansion, which caused the gas temperature to drop almost immediately to 234 K. This step served to turn all cloud droplets into ice crystals (Wagner et al., 2017). If we had continued with a moderate pumping speed, only a smaller fraction of the cloud droplets would have frozen, because ice crystals formed in slightly colder parts of the chamber volume would have grown at the expense of surrounding cloud droplets due to the Wegener-Bergeron-Findeisen process. Instead, the super-expansion caused most of the pristine SOA aerosol particles to undergo atmospheric freeze-drying, so the resulting change in particle properties was more apparent in the AIDA measurement data. The nucleated ice crystals showed a much wider distribution of optical diameters in the OPC1 data, but N_{OPC1} remained constant throughout the super-expansion, emphasizing that the goal of freezing all cloud droplets was achieved. With the super-expansion, the relative humidity immediately dropped from $RH_{liq} = 100\%$ to $S_{ice} = 1$. This drying step induced the vitrification of the SOM material that had been rejected from the ice lattice.

Shortly after the super-expansion, we simulated the outflow region of a deep convective cloud system by refilling the chamber with dry synthetic air to sublimate the ice phase, leaving behind the cloud-processed, porous SOA particles (fourth vertical line in Figure 4). Their modified optical properties compared to the pristine, compact SOA particles were evident from the OPC1 and SIMONE data. The porous SOA particles scattered much less light in the 178° detection channel of SIMONE, resulting in a five-fold increase in the forward-to-backward scattering ratio σ. A decrease in the intensity of backscattered light for porous particles has also been observed in light scattering simulations (Halder et al., 2018; Kahnert et al., 2014). The scattering cross sections of the porous SOA particles also became significantly smaller at scattering angles between 78 and 102°, the angular measurement range of the OPC1, as the fraction of the total SOA particle number concentration detected by the instrument (ratio N_{OPC1}/N_{CPC}) decreased from 6% before to 0.6% after the atmospheric freeze-drying step. Below we also show ESEM images that confirm the porous morphology of the particles.

In an optimal experiment, the chamber temperature would have been dynamically lowered to release the cloud-processed SOA particles into a colder atmosphere. In reality, however, the AIDA gas temperature relaxed to 243 K after the expansion cooling stopped, that is, to the temperature of the chamber walls, and for further characterization of the freeze-dried particles it must be ensured that they retain their porous structure under such conditions. In our previous experiments, we observed a slight restructuring of the SOA particles at 243 K, as evidenced for example, by an increase in N_{OPC1} over time after the freeze-drying step (Wagner et al., 2017). There, we had prepared AIDA with the inner walls of the chamber coated with ice. The cloud-processed SOA particles therefore had relaxed to an environment with $T = 243$ K and $RH_{liq} > 70\%$. To help stabilize the porous structure in the present study, we used the modified humidification procedure described in Section 2.2, avoiding the ice layer on the chamber walls. By partially pumping out the moist air and replacing it with dry air, RH_{liq} was reduced to about 62% after the freeze-drying experiment, with the ulterior motive that the lower relative humidity would further increase particle viscosity and thereby stabilize the porous structure. Figure 5 shows the long-term trend of the two AIDA measurement data, which are the most robust indicators of the porous particle structure, namely N_{OPC1} and σ. It can be seen that these two variables have changed very little in the hours following the initial expansion cooling run. During this time, the porous particles could be comprehensively characterized by taking ESEM samples, measuring their effective density, and investigating their ice nucleation ability at different temperatures in the cirrus regime with the CFDCs. This is exactly the experimental improvement mentioned in the introduction and means that we used AIDA exclusively for the generation and long-term stabilization of the porous SOA particles.

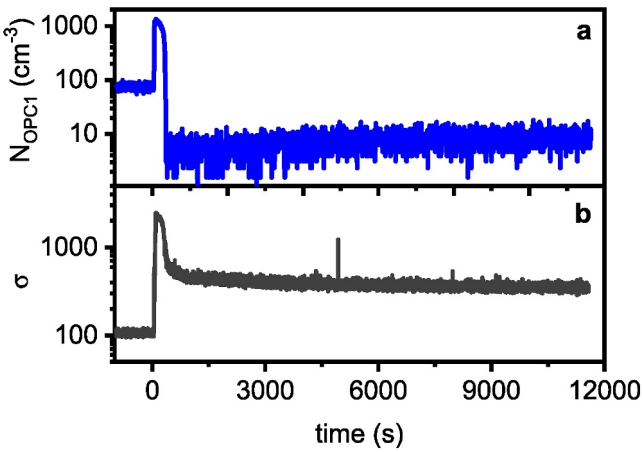

Figure 5. Long-term trend of the total particle count rate measured by the OPC1 (part a) and the forward-to-backward (2°-to-178°) scattering ratio measured by the SIMONE instrument (part b) during the atmospheric freeze-drying experiment with pure SOA particles shown in Figure 4.

The fact that the AIDA chamber was used only as a reservoir tank provided the opportunity for a further processing step in our experiments. After characterizing the porous SOA particles, we intentionally increased the relative humidity to reduce the viscosity and allow the particles to re-collapse into a more compact structure. This was done by means of another expansion cooling run, the measurement data of which are shown in Figure 6. About 105 s after the start of the pumping, when the gas temperature had dropped to 239 K and RH_{liq} had increased to 85% (second vertical line), the SOA particles "reappeared" in the OPC1 data, that is, N_{OPC1} increased, and at the same time the forward-to-backward scattering ratio σ decreased. Thus, we observed the reverse trends compared to the initial freeze-drying step, indicating that the opposite process, namely the re-compaction of the SOA particles, had taken place. With continued pumping, the re-compacted SOA particles were finally activated into micron-sized cloud droplets (third vertical line in Figure 6). The expansion run was then immediately stopped before the cloud droplets could freeze, and after water evaporation the re-compacted SOA particles were analyzed in a further characterization phase.

Therefore, our experiments included a total of three characterization phases, (1) pristine, compact SOA particles, (2) freeze-dried, porous SOA particles, and (3) re-compacted SOA particles. In Figure 7 we show exemplary ESEM images of SOA particles specifically sampled in one of these three characterization periods in combination with the effective density measurements with the tandem DMA-APM system. The ESEM images clearly reveal the fluffy morphology of the freeze-dried SOA particles, while the pristine particles are near-spherical in shape. One of the selected images from stage 2

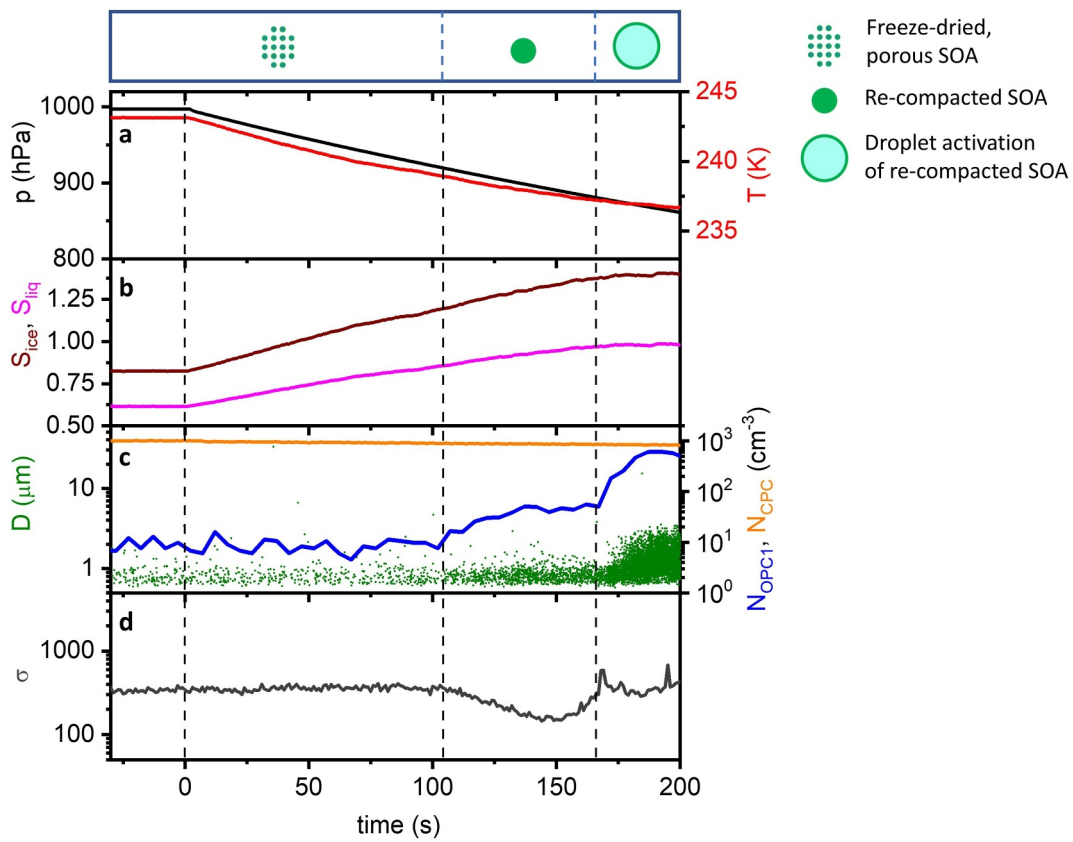

Figure 6. Re-compaction of freeze-dried, porous SOA particles by means of an AIDA expansion cooling experiment. The individual parts show the same measurement data as in Figure 4. The pictograms at the top are again a representation of the processing of the particles throughout the experiment, which is described in detail in Section 3.

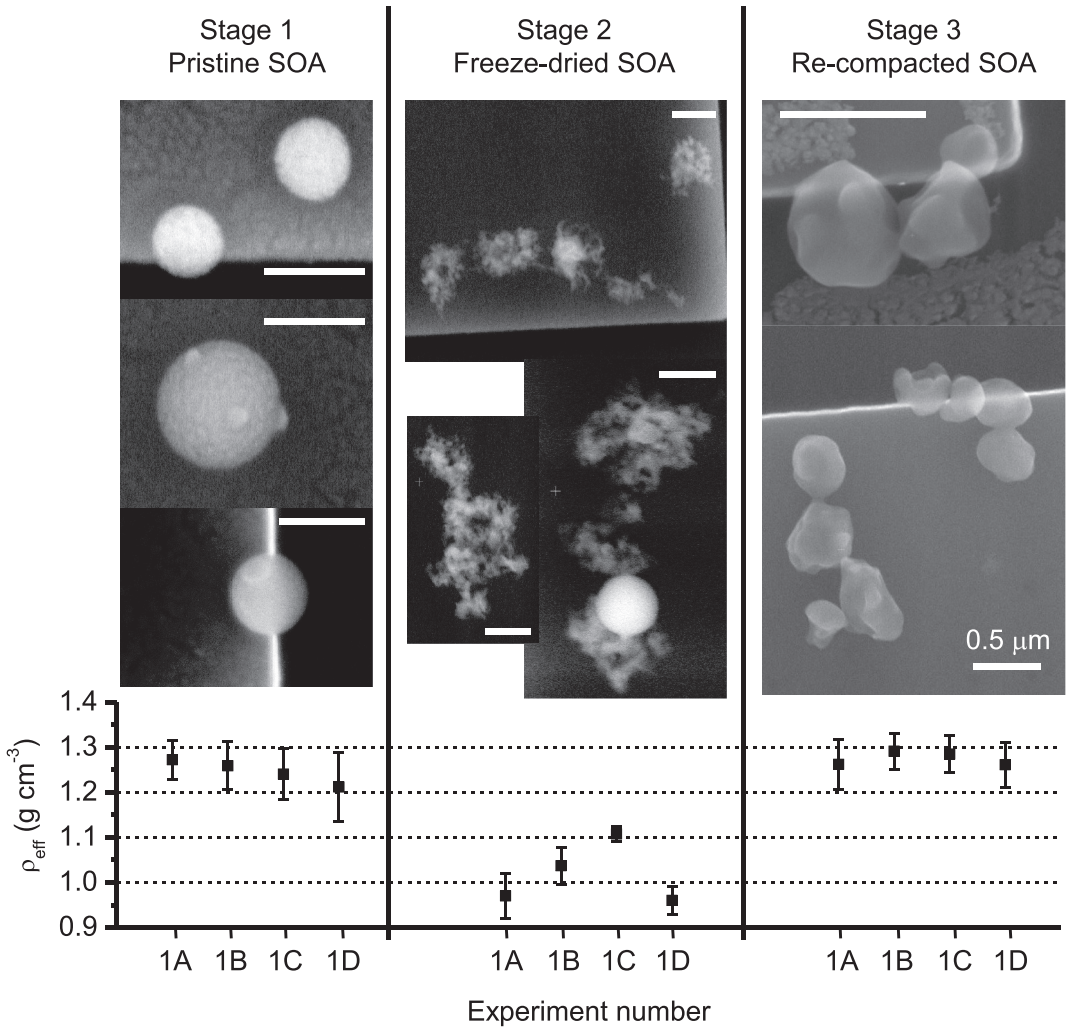

Figure 7. ESEM images and effective density measurements (ρ_{eff}) for the three different stages of the atmospheric freeze-drying experiments with pure SOA particles (experiment type 1, Table 1, individual runs A–D). ρ_{eff} was measured for each stage in all four experiments performed and is presented as an average for particle mobility diameters between 275 and 400 nm. Due to time constraints, ESEM sampling and analysis was performed for only one selected stage during each experiment. Therefore, the ESEM images are from different sub-runs of type 1 experiments. The images were taken at different magnifications, and the horizontal white bar in each image corresponds to a length of 0.5 µm.

also shows an unprocessed, spherical SOA particle, but the proportion of these was ≤5% of the total particle ensemble after freeze-drying. During the re-compaction step, the SOA particles did not have time to fully relax to a spherical geometry, and they appear slightly bulbous, but the fluffy branches have completely disappeared. Accordingly, the effective density of the particles, which had temporarily decreased to about 1 g cm^{-3} in stage 2, returned to the range of 1.25–1.30 g cm^{-3} of the pristine SOA particles. Adler et al. (2013) observed a greater decrease in density after freeze-drying, and we cannot exclude the possibility that the porous particles were already partially re-collapsed during our DMA-APM measurements, as these were performed at room temperature, where the SOA particles may have left the glassy region of the phase diagram even at low RH_{liq} (Koop et al., 2011). This emphasizes the particular need for sampling at low temperatures for the ESEM analysis and the precautions taken for the ice nucleation measurements, where we used a cooled sampling line from the AIDA chamber to the inlet of the CFDCs.

We now proceed to describe the ice nucleation behavior of the pure SOA particles in the three different experimental stages (Section 4.1). The processing of the SOM-coated zeolite and CFA particles was performed in essentially the same manner as shown in Figures 4 and 6 for the pure SOA particles, that is, including both the

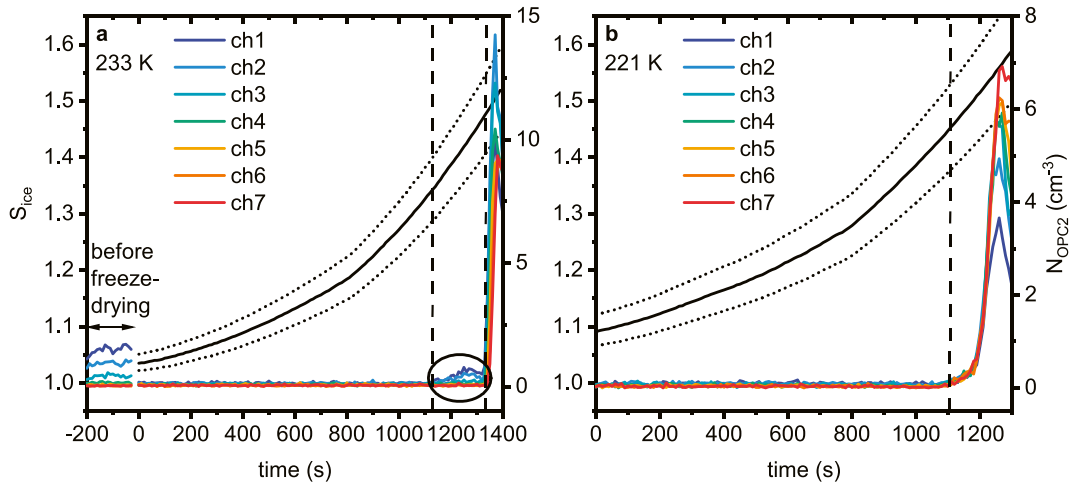

Figure 8. Shape change and ice nucleation behavior of freeze-dried SOA particles probed in INKA humidity scans at 233 K (part a) and 221 K (part b) (stage 2, Figure 7). The black lines associated with the left *y*-axes show the increase in S_{ice} during the humidity ramps started at time zero, with the dotted lines representing its uncertainty. The other colored lines are linked to the right *y*-axes and indicate the count rate in individual size channels of the OPC2 connected to the outlet of the CFDC (Figure 1). The pre-zero time range in part a shows the count rates in these size channels for pristine, compact SOA particles that were sampled by INKA at $S_{ice} \approx 1$ prior to the atmosphere-freeze drying expansion run in the AIDA chamber (stage 1). In part a, the two vertical dashed lines denote the particle re-compaction step and the ice nucleation onset, respectively, while the single vertical dashed line in part b denotes the ice nucleation onset. See text for details.

freeze-drying and the re-compaction step. Peculiar experimental details that are relevant to these internally mixed particle types will be discussed in the context of the respective ice nucleation measurements in Section 4.2.

4. Results of the Ice Nucleation Measurements

4.1. CFDC Measurements With Pure SOA Particles

We start the discussion with two examples from the CFDC measurements, where the freeze-dried SOA particles in characterization stage 2 were probed with INKA at 233 and 221 K (Figure 8). The data show the increase in S_{ice} during the humidity ramp and the evolution of the particle count rate in seven different size channels (ch) of the OPC2 connected to the outlet of INKA (Figure 1). Ch1–Ch4 cover the submicron size range with a detection limit of about 0.5 μm (Bertozzi, 2021), and detect not only smaller hydrometeors but also the larger tail of the SOA particle size distribution, while channels ≥5 are sensitive only to cloud droplets and ice crystals with sizes larger than 1 μm. The pre-zero time range added to Figure 8a shows the count rate in the selected size channels for the pristine, compact SOA particles sampled by INKA at $S_{ice} \approx 1$ prior to the freeze-drying expansion run in characterization stage 1. For better comparison, these data were corrected for the particle dilution that occurred during the later freeze-drying run. As in the AIDA measurements, the freeze-dried SOA particles are much less visible in the OPC data, and the count rates in ch1–ch4 are initially reduced to almost zero. The second vertical line at $S_{ice} = 1.48$ in the INKA scan at 233 K marks the onset of ice nucleation during the humidity ramp. This is indicated by the strong increase in the count rate of all size bins, including those with channel numbers ≥5. However, before the onset of ice formation, a clear increase in the count rate of the smaller size channels can be observed starting at $S_{ice} = 1.34$ ($RH_{liq} = 91\%$) (first vertical line in Figure 8a, also highlighted by the black circle). We interpret this in the same way as in the humidity-induced re-compaction experiment performed in AIDA at 243 K (Figure 6). The viscosity of the SOA particles is reduced by the increase in relative humidity and they reappear in the smaller OPC2 size channels due to the collapse of the porous structure. Kinetic limitations due to the short residence time of the particles in the CFDC of about 10 s could be the reason why the count rates do not fully recover to the values before freeze-drying, indicating only partial but not complete re-compaction. Our observed onset conditions for re-compaction at $S_{ice} = 1.34$ and 233 K are in good agreement with those found for water uptake by α-pinene-derived SOA particles at $S_{ice} = 1.31$ and 236 K (Charnawskas et al., 2017), indicating their liquefaction. The re-compaction step in our study occurred at a higher relative humidity than the coalescence of non-spherical α-pinene SOA agglomerates into spheres observed at 235 K and 80% RH_{liq} in cloud chamber

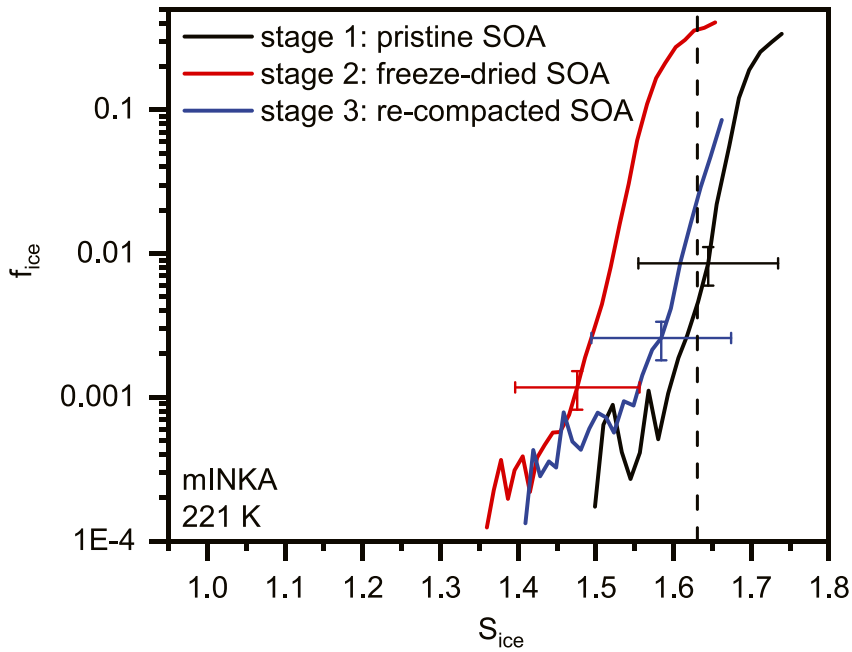

Figure 9. Ice activation spectra measured with mINKA at 221 K showing the evolution of the ice-active fraction, f_{ice}, as a function of the ice saturation ratio, S_{ice}, for SOA particles in the three different characterization stages defined in Figure 7. Horizontal and vertical errors bars reflect the estimated uncertainties for S_{ice} and f_{ice}, respectively, as described in Section 2.1. The vertical dashed line indicates water-saturated conditions at 221 K. f_{ice} values less than 1, even in the case where water saturation was nominally clearly exceeded (stage 1), could have several causes: The uncertainty in the calculation of S_{ice} at the aerosol lamina and possible perturbations of the laminar flow could mean that not all aerosol particles have actually experienced water-supersaturated conditions to become activated. Also, the hydrophobicity of the SOA particles may require conditions well above water saturation to activate all particles.

experiments at CERN (Järvinen et al., 2016). Variations in SOA production conditions can change the viscosity of the particles and be the cause of this difference (Grayson et al., 2016; Petters et al., 2019). Another reason could be the much shorter observation time in the CFDC compared to the cloud chamber experiments of Järvinen et al. (2016), where coalescence occurred on a time scale of 10 min.

There are two important conclusions that can be drawn from the observed re-compaction step in Figure 8a. First, the setup with the cooled sampling line from the AIDA chamber was helpful in preserving the morphology because the particles were obviously still porous when they entered the CFDC. Second, the porous structure was not stable at 233 K during the humidification ramp, so that the ice nucleation mode starting at $S_{ice} = 1.48$ can likely be interpreted as homogeneous freezing of the partially re-collapsed and liquefied SOA particles. In contrast, the INKA data at 221 K showed no evidence of such particle re-compaction prior to the onset of ice nucleation (indicated by the first vertical line in Figure 8b). Since the particles remained porous during the humidity scan, it can be investigated whether their ice nucleation ability is different from that in characterization phase 1, when they were still compact.

Figure 9 shows the ice activation spectra recorded with mINKA at 221 K during one of the four type 1 experiments, where measurements were performed in all three different characterization stages. A small reversible change in the ice nucleation behavior can be seen. The f_{ice} versus S_{ice} curve of the porous SOA particles is horizontally shifted to lower S_{ice} values by about 0.1 compared to that of the pristine SOA particles, and returns almost to the original values for the re-compacted particles. The slight change in the activation curves is similar to the absolute uncertainty of S_{ice} in the CFDC measurements, which is primarily due to the uncertainties in the temperature and the gap width between the two cylindrical walls of the instrument, which depends on the thickness of the deposited ice layers (Bertozzi, 2021; Schiebel, 2017). However, since the CFDC scans were performed consecutively with a well-conditioned instrument and no re-icing was required in between, we assume that the relative trend in the f_{ice} versus S_{ice} curves is a robust result. Moreover, the data in Figure 9 are only a

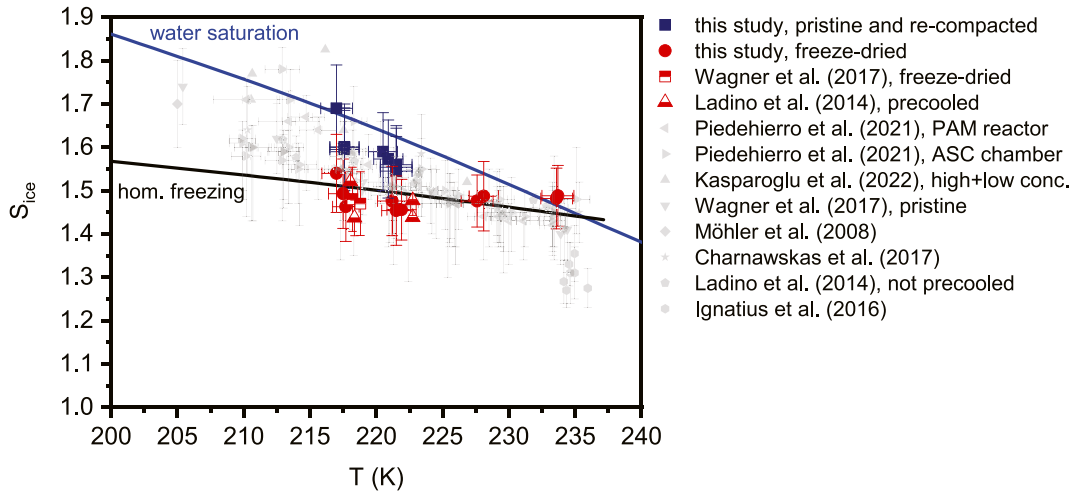

Figure 10. Overview of temperature-dependent onset conditions for ice formation by α-pinene-derived SOA particles. The dark-blue squares are the S_{ice} thresholds for the activation of 0.1% of the aerosol population from our current experiments with pristine and re-compacted particles (stage 1 and 3), while the red circles represent the corresponding values for the porous, freeze-dried particles of characterization stage 2. The other two red-colored symbols denote the nucleation onsets (f_{ice} = 0.1%) from our earlier experiments, where the freeze-dried particles were cooled to 223 K in the AIDA chamber and examined for their ice nucleation ability in an expansion cooling run (Wagner et al., 2017), and from the CFDC measurements by Ladino et al. (2014), where the SOA particles were precooled to 233 K before entering the CFDC. Gray symbols refer to ice nucleation onsets from other measurements with pristine, unprocessed SOA particles formed from α-pinene and correspond to activated fractions of 0.1% to 1%. The black line denotes the threshold for the homogeneous freezing of aqueous solution droplets (Koop et al., 2000), and the blue line represents water-saturated conditions (Murphy & Koop, 2005).

representative example of the overall picture that emerges from all the experiments carried out and is shown in Figure 10.

Figure 10 displays the ice nucleation onsets for an activated fraction of 0.1%, grouped in dark-blue squares for the characterization periods with pristine and re-compacted SOA particles (stages 1 and 3) and in red circles for the freeze-dried porous particles of characterization stage 2. The exemplary result of Figure 9 is confirmed, and a small average decrease of 0.1 in S_{ice} is observed at 221 and 217 K, that is, in the temperature range where the freeze-dried particles retained their porous network and did not re-collapse during the CFDC humidity scan (Figure 8). The S_{ice} onsets for the pristine and re-compacted SOA particles lie midway between the homogeneous freezing line of aqueous solution droplets and water-saturated conditions (black and blue lines in Figure 10, respectively). This is precisely the region where most previous measurements also locate the onset of ice nucleation for pristine, α-pinene-derived SOA particles (gray symbols in Figure 10), with the study by Ignatius et al. (2016) being the only notable exception. The nucleation onsets for the porous SOA particles are at or even slightly below the homogeneous freezing threshold, and are in good agreement with the two data points from our previous study where we cooled the freeze-dried particles to 223 K in the AIDA chamber to study their ice nucleation ability in an expansion cooling run (red, half-filled squares in Figure 10, original data in Figure 8 of Wagner et al., 2017). We also chose the red color coding to represent the subset of CFDC measurements by Ladino et al. (2014), where the SOA particles were precooled to 233 K before entering the diffusion chamber (half-filled triangles in Figure 10). Interestingly, this precooling resulted in a similar small decrease in the ice nucleation onsets of the SOA particles as we observed in our freeze-drying experiments. This could indicate that the precooled particles were subjected to similar ice cloud processing as in our experiments, which Ladino et al. (2014) could not rule out as the relative humidity was not measured during the cooling step.

Since a reduction in the S_{ice} onsets is observed after the atmospheric freeze-drying step, it seems justified to classify this as a heterogeneous ice nucleation mode, but one that occurs in close proximity to the conditions under which aqueous solution droplets would form ice homogeneously. To put it simply, the porous SOA particles are rather inefficient INPs. In the following, we will use model simulations for cylindrical pores to analyze the observed ice nucleation behavior in the context of the PCF mechanism. As a note of caution, we want to

emphasize that this can only be considered as a rough approximation, since the fluffy, ice-cloud processed SOA particles do not exhibit well-defined pore geometries or dimensions in their highly irregular structure. The inverse Kelvin equation can be used to calculate the onset RH_{liq} of condensation of supercooled water in a circular capillary of given diameter and wettability as expressed by the contact angle θ of water on the pore material (David et al., 2020; Mahrt et al., 2020). By setting this RH_{liq} threshold equal to the measured S_{ice} onsets of the processed SOA particles, it is possible to derive the pore characteristics that could account for the observed ice nucleation behavior if PCF were the underlying ice formation pathway. Assuming that the material is perfectly wettable with $\theta = 0°$, a pore diameter of 30 nm would be obtained, while a higher contact angle of $\theta = 60°$ would be consistent with the presence of 15 nm-sized pores. An efficient and well known INP type under cirrus conditions are mineral dust particles, where high heterogeneous ice nucleation ability (i.e., ice nucleation active surface site densities $> 10^{10}$ m^{-2}) can already be observed at S_{ice} values as low as 1.2 for temperatures below 220 K (Ullrich et al., 2017). If the freeze-dried SOA particles were to compete with this abundant INP type, that is, also nucleate ice efficiently at $S_{ice} = 1.2$, the calculation in terms of the PCF mechanism presented above would require the presence of pore diameters of about 12 to 6 nm for contact angles between 0 and 60°. Apparently, such smaller mesopores are absent in the rather open network structure of the fluffy SOA particles and, together with the poor wettability of the organic material, could explain why the PCF mechanism is not particularly effective for this class of particles.

Apart from the explanation in terms of the PCF mechanism, the slightly improved ice nucleation ability of the porous SOA particles could be considered as a pre-activation phenomenon due to the preceding ice cloud-processing. In this line of reasoning, the ice crystals temporarily formed in the atmospheric freeze-drying step could have left a footprint of the ice configuration in the porous organic network that slightly improves the ice nucleation ability compared to the pristine SOA particles (Vali, 2008). Rather than a pre-activation effect, the increased surface area of the freeze-dried, fluffy SOA particles alone could provide a greater number of sites for heterogeneous ice nucleation compared to the pristine, compact SOA particles. Whichever interpretation is correct, our results provide a first indication that the recommendation of Kasparoglu et al. (2022) mentioned in the introduction, that is, glassy SOA particles can be considered inactive for heterogeneous ice nucleation in models, is also applicable to ice-cloud processed, fluffy particle types. However, we cannot yet generalize this result based on just one SOA precursor (i.e., α-pinene) studied. Different precursors, and different SOM production conditions for an individual precursor type, can change the O:C ratio and viscosity of the particles (Grayson et al., 2016; Petters et al., 2019). During the atmospheric freeze-drying process, the viscosity of the SOM can affect the way in which the phase-separated, organic phase is redistributed on the temporarily formed ice crystal, ultimately determining the network structure and surface area of the fluffy particles left behind after the ice sublimates. This in turn could lead to a different ice nucleation ability than observed in our study. In the next section, we focus on the experiments with the internally mixed particle types, where, in contrast to the pure SOA particles, atmospheric freeze-drying had a strong influence on the ice nucleation behavior.

4.2. CFDC Measurements With Internally Mixed Zeolite/SOM and CFA/SOM Particles

We chose the zeolite particles as a first proxy for a very ice-active INP and investigated whether an initially compact coating layer of SOM, which deactivates the intrinsic ice nucleation ability of the particles, would change its structure during atmospheric freeze-drying such that the coated particles become more ice-active again. The green line in Figure 11a shows the ice activation spectrum of pure zeolite particles from the reference experiment type 4 (Table 1, direct injection into the AIDA chamber) measured with INKA at 228 K. The onset of ice nucleation occurred at $S_{ice} = 1.07$, and before the ice saturation ratio reached a value of 1.15, more than 10% of the aerosol population had already become ice-active. This superior ice nucleation ability of the zeolite particles of type CBV400 can be explained by the PCF mechanism in view of the presence of small mesopores in the size range from 4 to 20 nm. Again using the inverse Kelvin equation, the observed ice nucleation threshold would correspond to the onset of capillary condensation in a 4.5 nm pore with $\theta = 60°$ or in a pore with a diameter of 9 nm in the case of perfect wettability with $\theta = 0°$.

In experiment type 2, we first injected the zeolite particles into the APC vessel, coated them with SOM from the ozonolysis of α-pinene, transferred them to the AIDA chamber and measured their ice activation spectrum at 228 K with INKA. The black line in Figure 11a shows an almost complete suppression of the intrinsic ice nucleation ability of the zeolite particles by the pristine, compact SOM coating, where f_{ice} did not exceed 0.1% even when S_{ice} was increased to 1.4 and beyond. Note that f_{ice} was calculated with respect to the mode of the

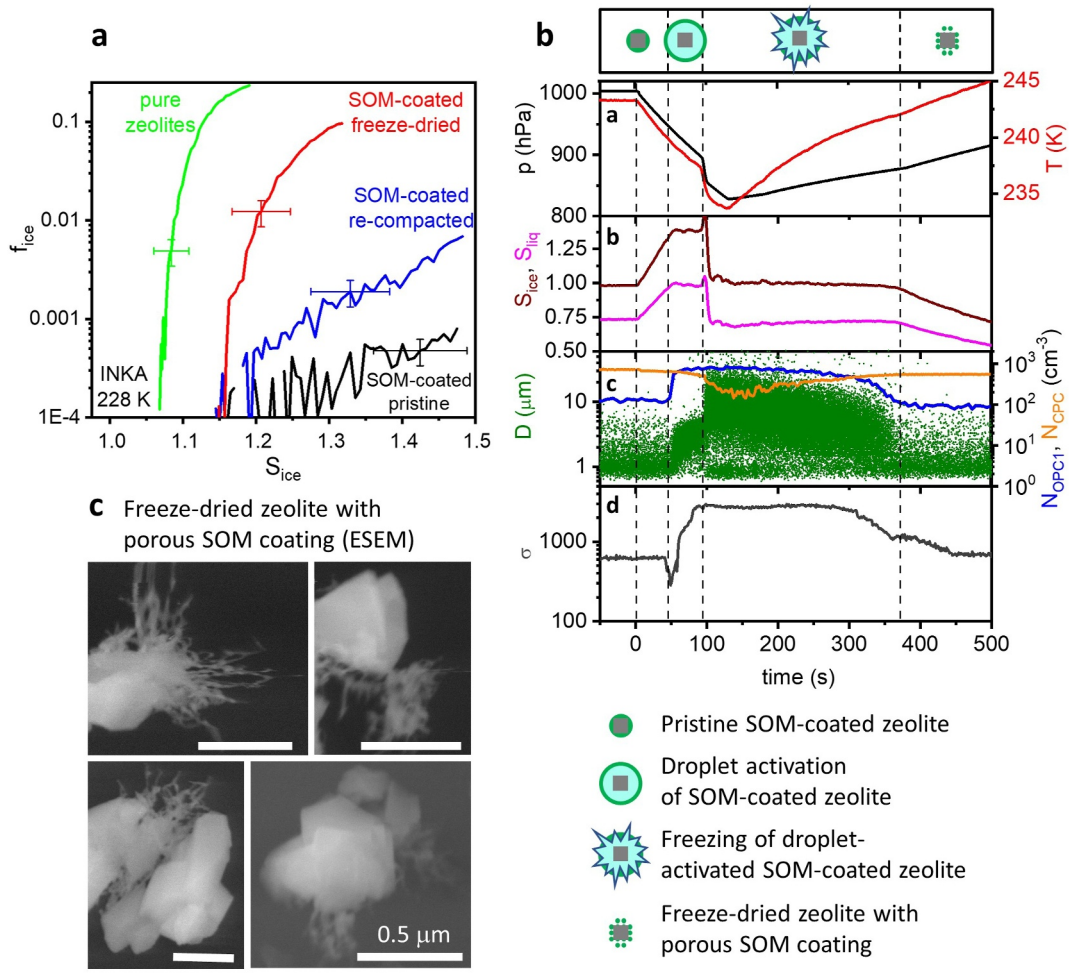

Figure 11. Freeze-drying experiment with SOM-coated zeolite particles of type CBV400. Part (a) Ice activation spectra measured with INKA at 228 K showing the evolution of the ice-active fraction, f_{ice}, as a function of the ice saturation ratio, S_{ice}, for the reference experiment with the pure zeolite particles (type 4, Table 1) and the SOM-coated zeolite particles (type 2, Table 1) in the three different characterization stages. (b) AIDA measurement data during the atmospheric freeze-drying experiment with the SOM-coated zeolite particles. The processing of the particles during the experiment is symbolized by the pictograms at the top. The individual subparts a–d show the same measurement data as in Figure 4. (c) ESEM images of the freeze-dried, SOM-coated zeolite particles in characterization stage 2. The horizontal white bar in each image corresponds to a length of 0.5 µm.

SOM-coated zeolite particles only, ignoring the mode of the pure, ice-inactive SOA particles that were additionally formed during coating in the APC chamber (Figure 2b). We then performed the atmospheric freeze-drying experiment similar to the one with pure SOA particles, and the AIDA measurement data are shown in Figure 11b. In contrast to the data for pure SOA shown in Figure 4, we observed a very small heterogeneous ice formation mode with $f_{ice} < 0.5\%$ before the super-expansion was initiated to convert the cloud droplets into ice crystals by homogeneous freezing. This mode can be attributed to immersion freezing by the droplet-activated, SOM-coated zeolite particles. The two diagnostic measurements for the formation of porous SOA particles from Figure 4, namely the increase in the forward-to-backward scattering ratio σ and the decrease in the ratio N_{OPC1}/N_{CPC} are not evident in the data of Figure 11b, indicating that the light-scattering properties of the SOM-coated particles, as measured by the OPC1 and the SIMONE instrument, did not change much after freeze-drying. After freeze-drying, however, a clear change in the ice nucleation ability could be observed (red line in Figure 11a), that is, the ice activation spectrum shifted, albeit not completely, in the direction of the spectrum measured for the pure, uncoated zeolite particles in the reference experiment. Specifically, ice formation began at $S_{ice} = 1.16$, with a further rapid increase in f_{ice} with increasing S_{ice}, although somewhat less steep than for the pure zeolite particles.

In the characterization stage 2 after freeze-drying, we also sampled the particles with the liquid nitrogen-cooled transfer shuttle, and some representative ESEM images are shown in Figure 11c. One can see the rather compact body of the CBV400 zeolite particles consisting of several aggregated grains (similar to the images shown in Figure 1 in Wagner et al. (2016)) and some ramified, fibrous material that has detached from the surface. The latter is the organic coating material that has been restructured by the ice cloud-processing in the atmospheric freeze-drying experiment, and is partially detached from the body of the zeolite particles instead of forming a compact coating layer. The recommendation by Kasparoglu et al. (2022) to treat SOM-coated dust particles as ice-inactive with respect to cirrus formation in models is therefore only valid for particles with a pristine, compact coating layer, but not for particles that have been processed in deep convective cloud systems, which can make them efficient INPs again. Since the atmospheric freeze-drying experiments with pure SOA particles showed only a slight increase in the ice nucleation ability, we suggest that the strong activation of the SOM-coated zeolite particles is not related to the fibrous, fluffy organic material providing new active sites, but rather to the re-exposure of previously concealed active sites on the zeolite surface. The light scattering properties of the SOM-coated zeolite particles are apparently mainly determined by the bulk of the zeolite aggregates and are not sensitive to whether the coating material forms a thin layer or partially protrudes as thin, fluffy material from the surface, so that the two diagnostic measurements mentioned above did not change much during freeze-drying. Note that even after the sublimation of most of the ice crystals formed in the freeze-drying step (fourth vertical dashed line in Figure 11b), σ still shows some variation, reaching a constant value only at $t = 450$ s. These variations could be due to particle restructuring or, more likely, still ongoing sublimation of the few very large ice crystals formed by immersion freezing early in the experiment.

After the characterization stage 2, we performed the re-compaction step by temporarily increasing the relative humidity in the AIDA chamber, as shown in Figure 6 for the pure SOA particles, so that the fibrous, detached SOM material could become less viscous and partially redistribute on the zeolite surface. Indeed, the INKA measurement confirmed a significant deterioration of the ice nucleation ability after re-compaction, when the zeolite particles became more homogeneously coated with SOM again (blue line in Figure 11b). As noted in the caption to Figure 7, time constraints prevented us from performing another round of low-temperature particle sampling and ESEM characterization to directly demonstrate that the fibrous structure of the SOM material had disappeared after re-compaction.

Figure 12 is structured identically to Figure 11 and shows the measurement data for the experiments with pure (type 5) and SOM-coated CFA particles (type 3, Table 1). Part c includes reference electron microscope images of bare, uncoated CFA particles recorded in Umo et al. (2019). These particles exhibit a variety of morphologies, ranging from rather compact grains with a surface of spongy material to very open-structured agglomerates. They acted as very efficient INPs under cirrus conditions with an ice nucleation onset as low as $S_{ice} = 1.1$ at 225 K (green line, Figure 12a, reference experiment type 5). In Section 2.2, we found that coating the CFA particles with SOM in the APC chamber led to a reduction in the width of the particle size distribution rather than an increase in the mean diameter. The condensable organic material obviously filled the inner cavities of the CFA particles rather than forming an outer coating layer as in the zeolite particles, which have a more compact body apart from the internal mesoporous network. The SOM coating led to a significant deterioration in the ice nucleation ability compared to the bare CFA particles (Figure 12a, black line), although a certain residual activity with f_{ice} between 0.0001 and 0.001 was still observed at $S_{ice} < 1.4$, probably because the mass of the organic material was not yet sufficient to completely block or fill all active sites in the cavities of the particles. Similar to the zeolite particles, freeze-drying restored the intrinsic ice nucleation ability of the CFA particles to a significant degree by moving the nucleation onset back to $S_{ice} = 1.15$ (Figure 12a, red line). The ESEM images of the freeze-dried, SOM-coated CFA particles collected in characterization phase 2 show an extremely irregular, ruptured morphology (Figure 12c). One can see the fluffy organic material distributed among the fragments of CFA, as if the entire particles had been torn apart to some degree by the ice cloud-processing. While freeze-drying did not significantly modify the optical properties of the SOM-coated zeolite particles (Figure 11b), the ice cloud-processed CFA/SOM particles showed a clear change in the OPC1 and SIMONE data (Figure 12b), indicating their highly irregular morphology: The ratio N_{OPC1}/N_{CPC} decreased by a factor of 3 after freeze-drying, while the forward-to-backward scattering ratio σ increased by a factor of 2. Due to the strong structural change during freeze-drying, it is unlikely that the subsequently conducted re-compaction step could fully restore the original particle morphology of the SOM-coated CFA particles. The mINKA measurement after re-compaction (Figure 12c, blue line) showed a reduction in the ice nucleation ability, but clearly less pronounced than in the case of the zeolite/

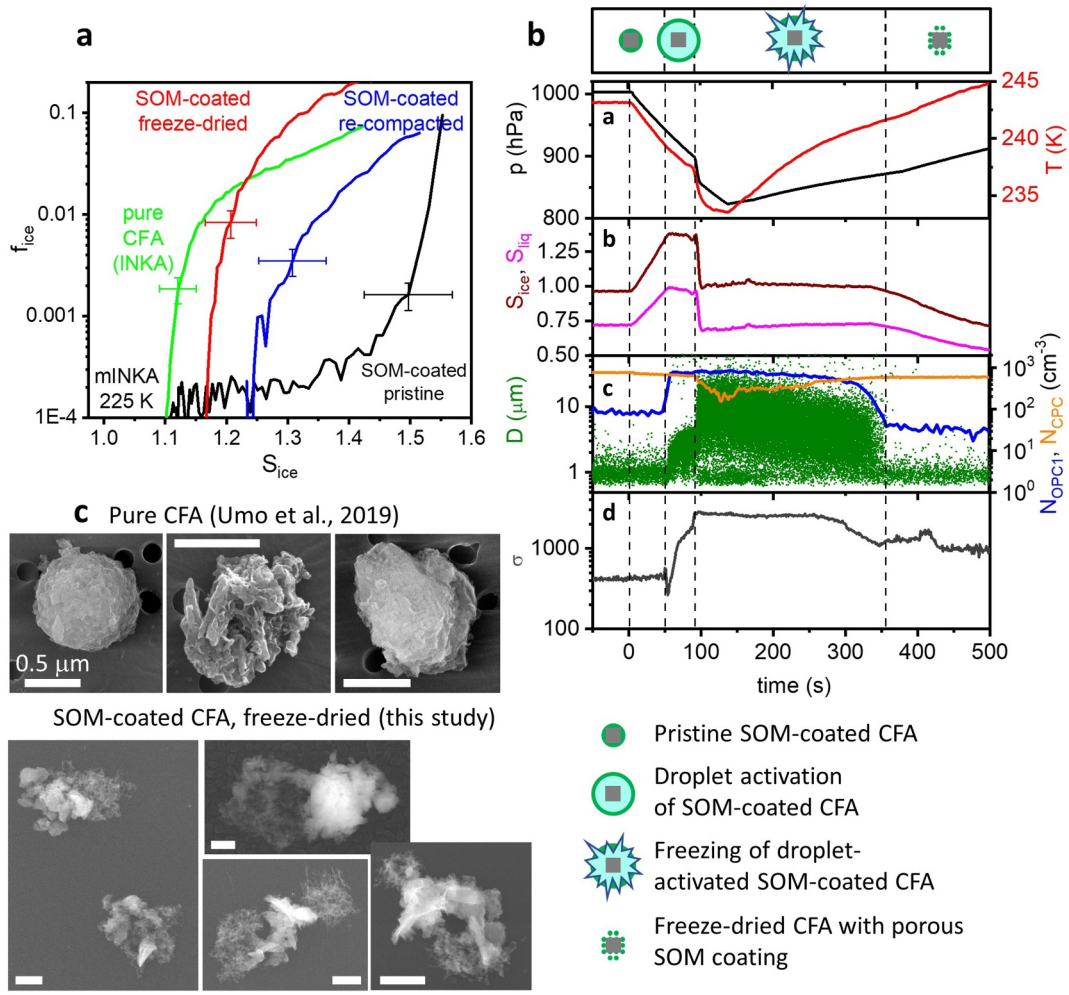

Figure 12. Freeze-drying experiment with SOM-coated CFA particles. Part (a) Ice activation spectra at 225 K showing the evolution of the ice-active fraction, f_{ice}, as a function of the ice saturation ratio, S_{ice}, for the reference experiment with the pure CFA particles (type 5, Table 1, measured with INKA) and the SOM-coated CFA particles in the three different characterization stages (type 3, Table 1, all measured with mINKA). (b) AIDA measurement data during the atmospheric freeze-drying experiment with the SOM-coated CFA particles. The processing of the particles during the experiment is symbolized by the pictograms at the top. The individual subparts a–d show the same measurement data as in Figure 4. (c) ESEM images of pure, uncoated CFA particles from the study of Umo et al. (2019) and of the freeze-dried, SOM-coated CFA particles in characterization stage 2 recorded in this work. The horizontal white bar in each image corresponds to a length of 0.5 µm.

SOM particles. Thus, the ice-cloud processed CFA/SOM particles remained rather efficient INPs even after a transient increase in RH that reduced the viscosity of the organic material, and did not revert to an idealized core (CFA)-shell (SOM) morphology that could be considered as ice-inactive.

5. Summary and Outlook

We conducted an experimental study on how porosity affects the ice nucleation behavior of pure SOA particles under cirrus conditions and extended it to two internally mixed particle types consisting of zeolite/SOM and CFA/SOM. In all experiments, the condensable organic matter was generated by the ozonolysis of α-pinene. The AIDA cloud chamber was used to simulate particle processing in a deep convective cloud system, resulting in the transformation of compactly shaped SOA particles into a fluffy, porous morphology and the detachment or tearing of compact SOM coatings from the surface or internal voids of the zeolite and CFA particles. Ice nucleation measurements performed with CFDCs sampling the ice cloud-processed particles from the AIDA chamber showed that the porous SOA particles did not act as efficient INPs via the PCF mechanism, as the

nucleation onsets were only slightly reduced compared to their pristine, compact counterparts. Consequently, the presence of porous particles does not seem to change the prevailing understanding that has emerged from recent ice nucleation studies, namely that pure SOA particles can be considered ice-inactive in models to a good approximation (Kasparoglu et al., 2022). However, experiments with different precursors and SOM production conditions are needed to generalize this result. For the internally mixed particle types, we observed a partial recovery of the intrinsic heterogeneous ice nucleation ability of the zeolite and CFA particles after ice cloud-processing, which was initially largely suppressed by a pristine, compact SOM coating. We attribute this to the re-exposure of active sites on the surface of the two INPs, emphasizing that the general recommendation to treat even SOM-coated dust as ice-inactive in models only applies to particles with a uniform, compact coating layer, but not necessarily to cloud-processed particles where the structure of the coating may change. Although it refers to a different particle type (biomass burning aerosols) and temperature regime (mixed-phase cloud conditions), we may mention here another recent study that highlights the importance of considering the fate of coating layers during atmospheric aging with respect to the ice nucleation ability of the particles (Jahl et al., 2021). Here, several aging schemes were found to increase the ice nucleation ability of the biomass-burning aerosol particles, for example, by the removal of organic coatings from underlying, mineral-based ice-active sites.

We have introduced a new experimental procedure in which we used the AIDA chamber for the generation and long-term storage of the porous SOA particles, allowing for comprehensive characterization with different instruments. This also provided information about the viscosity change of the particles at low temperatures, as we were able to determine the RH_{liq} threshold at which the porous particles reverted to a more compact structure, similar to the experiments conducted by Järvinen et al. (2016). Extending this procedure to other atmospherically relevant precursors, such as isoprene (Claeys & Maenhaut, 2021), could provide relative trends in the viscosity of SOM generated from different molecules. A new LED-based solar simulator, recently installed in the AIDA chamber (Vallon et al., 2022), could be used to study the effect of photochemical aging on particle viscosity (Baboomian et al., 2022). As a final promising option for future experiments, a new dynamic cloud chamber called AIDAd was put into operation, which has a double chamber design in which the walls of the inner cloud chamber can be actively cooled (Alpert et al., 2023). This allows quasi-adiabatic cooling conditions to be achieved, overcoming the limitations of the classic AIDA chamber (Section 3) and providing a much wider dynamic temperature range for future cloud-processing studies.

Data Availability Statement

The processed data used to interpret the ice nucleation behavior of the SOA, zeolite/SOM, and CFA/SOM particles are the CFDC measurements shown in Figures 9–12 of the article. These data are available in KITOpen (RADAR4KIT repository) at https://doi.org/10.35097/e4xhczc6s8ebypv5 (Wagner et al., 2024).

Acknowledgments

We gratefully acknowledge the continuous support by all members of the Engineering and Infrastructure group of IMKAAF, in particular by Olga Dombrowski, Rainer Buschbacher, Tomasz Chudy, Jens Nadolny, Steffen Vogt, and Georg Scheurig. This work has been funded by the Helmholtz-Gemeinschaft Deutscher Forschungszentren as part of the program "Atmosphere and Climate." Marco Zanatta received funding from the DFG (Deutsche Forschungsgemeinschaft, Grant 457895178). Open Access funding enabled and organized by Projekt DEAL.

References

Adler, G., Haspel, C., Moise, T., & Rudich, Y. (2014). Optical extinction of highly porous aerosol following atmospheric freeze drying. *Journal of Geophysical Research-Atmospheres*, *119*(11), 6768–6787. https://doi.org/10.1002/2013JD021314

Adler, G., Koop, T., Haspel, C., Taraniuk, I., Moise, T., Koren, I., et al. (2013). Formation of highly porous aerosol particles by atmospheric freeze-drying in ice clouds. *Proceedings of the National Academy of Sciences of the United States of America*, *110*(51), 20414–20419. https://doi.org/10.1073/pnas.1317209110

Alpert, P. A., Bernard, F., Connolly, P., Crabeck, O., George, C., Kaiser, J., et al. (2023). Application of simulation chambers to investigate interfacial processes. In J.-F. Doussin, H. Fuchs, A. Kiendler-Scharr, P. Seakins, & J. Wenger (Eds.), *A practical guide to atmospheric simulation chambers* (pp. 293–330). Springer International Publishing. https://doi.org/10.1007/978-3-031-22277-1_8

Baboomian, V. J., Crescenzo, G. V., Huang, Y., Mahrt, F., Shiraiwa, M., Bertram, A. K., & Nizkorodov, S. A. (2022). Sunlight can convert atmospheric aerosols into a glassy solid state and modify their environmental impacts. *Proceedings of the National Academy of Sciences*, *119*(43), e2208121119. https://doi.org/10.1073/pnas.2208121119

Baustian, K. J., Wise, M. E., Jensen, E. J., Schill, G. P., Freedman, M. A., & Tolbert, M. A. (2013). State transformations and ice nucleation in amorphous (semi-)solid organic aerosol. *Atmospheric Chemistry and Physics*, *13*(11), 5615–5628. https://doi.org/10.5194/acp-13-5615-2013

Berkemeier, T., Shiraiwa, M., Pöschl, U., & Koop, T. (2014). Competition between water uptake and ice nucleation by glassy organic aerosol particles. *Atmospheric Chemistry and Physics*, *14*(22), 12513–12531. https://doi.org/10.5194/acp-14-12513-2014

Bertozzi, B. (2021). *Ice nucleation ability of secondary aerosol particles at cirrus cloud conditions. (PhD)*. Karlsruhe Institute of Technology. https://doi.org/10.5445/IR/1000146739

Bertozzi, B., Wagner, R., Höhler, K., Saathoff, H., Möhler, O., & Leisner, T. (2024). Influence of the neutralization degree on the ice nucleation ability of ammoniated sulfate particles. *Journal of Geophysical Research: Atmospheres*, *129*(2), e2023JD040078. https://doi.org/10.1029/2023JD040078

Bertozzi, B., Wagner, R., Song, J., Höhler, K., Pfeifer, J., Saathoff, H., et al. (2021). Ice nucleation ability of ammonium sulfate aerosol particles internally mixed with secondary organics. *Atmospheric Chemistry and Physics*, *21*(13), 10779–10798. https://doi.org/10.5194/acp-21-10779-2021

Campbell, J. M., & Christenson, H. K. (2018). Nucleation- and emergence-limited growth of ice from pores. *Physical Review Letters*, *120*(16), 165701. https://doi.org/10.1103/PhysRevLett.120.165701

Charnawskas, J. C., Alpert, P. A., Lambe, A. T., Berkemeier, T., O'Brien, R. E., Massoli, P., et al. (2017). Condensed-phase biogenic–anthropogenic interactions with implications for cold cloud formation. *Faraday Discussions*, *200*(0), 165–194. https://doi.org/10.1039/C7FD00010C

Christenson, H. K. (2013). Two-step crystal nucleation via capillary condensation. *CrystEngComm*, *15*(11), 2030–2039. https://doi.org/10.1039/C3CE26887J

Claeys, M., & Maenhaut, W. (2021). Secondary organic aerosol formation from isoprene: Selected research, historic account and state of the art. *Atmosphere*, *12*(6), 728. https://doi.org/10.3390/atmos12060728

David, R. O., Fahrni, J., Marcolli, C., Mahrt, F., Brühwiler, D., & Kanji, Z. A. (2020). The role of contact angle and pore width on pore condensation and freezing. *Atmospheric Chemistry and Physics*, *20*(15), 9419–9440. https://doi.org/10.5194/acp-20-9419-2020

David, R. O., Marcolli, C., Fahrni, J., Qiu, Y. Q., Sirkin, Y. A. P., Molinero, V., et al. (2019). Pore condensation and freezing is responsible for ice formation below water saturation for porous particles. *Proceedings of the National Academy of Sciences of the United States of America*, *116*(17), 8184–8189. https://doi.org/10.1073/pnas.1813647116

Fahey, D. W., Gao, R. S., Möhler, O., Saathoff, H., Schiller, C., Ebert, V., et al. (2014). The AquaVIT-1 intercomparison of atmospheric water vapor measurement techniques. *Atmospheric Measurement Techniques*, *7*(9), 3177–3213. https://doi.org/10.5194/amt-7-3177-2014

Fukuta, N. (1966). Activation of atmospheric particles as ice nuclei in cold and dry air. *Journal of the Atmospheric Sciences*, *23*(6), 741–750. https://doi.org/10.1175/1520-0469(1966)023<0741:AOAPAI>2.0.CO;2

Grayson, J. W., Zhang, Y., Mutzel, A., Renbaum-Wolff, L., Böge, O., Kamal, S., et al. (2016). Effect of varying experimental conditions on the viscosity of α-Pinene derived secondary organic material. *Atmospheric Chemistry and Physics*, *16*(10), 6027–6040. https://doi.org/10.5194/acp-16-6027-2016

Halder, P., Deb Roy, P., & Das, H. S. (2018). Dependence of light scattering properties on porosity, size and composition of dust aggregates. *Icarus*, *312*, 45–60. https://doi.org/10.1016/j.icarus.2018.04.026

Hallquist, M., Wenger, J. C., Baltensperger, U., Rudich, Y., Simpson, D., Claeys, M., et al. (2009). The formation, properties and impact of secondary organic aerosol: Current and emerging issues. *Atmospheric Chemistry and Physics*, *9*(14), 5155–5236. https://doi.org/10.5194/acp-9-5155-2009

Haspel, C., & Adler, G. (2017). The concept of apparent polarizability for calculating the extinction of electromagnetic radiation by porous aerosol particles. *Journal of Geophysical Research: Atmospheres*, *122*(7), 3944–3952. https://doi.org/10.1002/2016JD026249

Higuchi, K., & Fukuta, N. (1966). Ice in capillaries of solid particles and its effect on their nucleating ability. *Journal of the Atmospheric Sciences*, *23*(2), 187–190. https://doi.org/10.1175/1520-0469(1966)023<0187:IITCOS>2.0.CO;2

Ignatius, K., Kristensen, T. B., Järvinen, E., Nichman, L., Fuchs, C., Gordon, H., et al. (2016). Heterogeneous ice nucleation of viscous secondary organic aerosol produced from Ozonolysis of alpha-Pinene. *Atmospheric Chemistry and Physics*, *16*(10), 6495–6509. https://doi.org/10.5194/acp-16-6495-2016

Jahl, L. G., Brubaker, T. A., Polen, M. J., Jahn, L. G., Cain, K. P., Bowers, B. B., et al. (2021). Atmospheric aging enhances the ice nucleation ability of biomass-burning aerosol. *Science Advances*, *7*(9), eabd3440. https://doi.org/10.1126/sciadv.abd3440

Janssen, A. H., Koster, A. J., & de Jong, K. P. (2002). On the shape of the mesopores in zeolite Y: A three-dimensional transmission electron microscopy study combined with texture analysis. *Journal of Physical Chemistry B*, *106*(46), 11905–11909. https://doi.org/10.1021/jp025971a

Järvinen, E., Ignatius, K., Nichman, L., Kristensen, T. B., Fuchs, C., Hoyle, C. R., et al. (2016). Observation of viscosity transition in alpha-Pinene secondary organic aerosol. *Atmospheric Chemistry and Physics*, *16*(7), 4423–4438. https://doi.org/10.5194/acp-16-4423-2016

Kahnert, M., Nousiainen, T., & Lindqvist, H. (2014). Review: Model particles in atmospheric optics. *Journal of Quantitative Spectroscopy and Radiative Transfer*, *146*, 41–58. https://doi.org/10.1016/j.jqsrt.2014.02.014

Kasparoglu, S., Perkins, R., Ziemann, P. J., DeMott, P. J., Kreidenweis, S. M., Finewax, Z., et al. (2022). Experimental determination of the relationship between organic aerosol viscosity and ice nucleation at upper free tropospheric conditions. *Journal of Geophysical Research: Atmospheres*, *127*(16), e2021JD036296. https://doi.org/10.1029/2021JD036296

Kilchhofer, K., Mahrt, F., & Kanji, Z. A. (2021). The role of cloud processing for the ice nucleating ability of organic aerosol and coal fly ash particles. *Journal of Geophysical Research: Atmospheres*, *126*(10), e2020JD033338. https://doi.org/10.1029/2020JD033338

Kiselev, A., Bachmann, F., Pedevilla, P., Cox, S. J., Michaelides, A., Gerthsen, D., & Leisner, T. (2017). Active sites in heterogeneous ice nucleation—The example of K-rich feldspars. *Science*, *355*(6323), 367–371. https://doi.org/10.1126/science.aai8034

Koehler, K. A., Kreidenweis, S. M., DeMott, P. J., Petters, M. D., Prenni, A. J., & Möhler, O. (2010). Laboratory investigations of the impact of mineral dust aerosol on cold cloud formation. *Atmospheric Chemistry and Physics*, *10*(23), 11955–11968. https://doi.org/10.5194/acp-10-11955-2010

Koop, T., Bookhold, J., Shiraiwa, M., & Pöschl, U. (2011). Glass transition and phase state of organic compounds: Dependency on molecular properties and implications for secondary organic aerosols in the atmosphere. *Physical Chemistry Chemical Physics*, *13*(43), 19238–19255. https://doi.org/10.1039/C1cp22617g

Koop, T., Luo, B. P., Tsias, A., & Peter, T. (2000). Water activity as the determinant for homogeneous ice nucleation in aqueous solutions. *Nature*, *406*(6796), 611–614. https://doi.org/10.1038/35020537

Kovács, T., & Christenson, H. K. (2012). A two-step mechanism for crystal nucleation without supersaturation. *Faraday Discussions*, *159*, 123–138. https://doi.org/10.1039/C2FD20053H

Ladino, L. A., Zhou, S., Yakobi-Hancock, J. D., Aljawhary, D., & Abbatt, J. P. D. (2014). Factors controlling the ice nucleating abilities of alpha-Pinene SOA particles. *Journal of Geophysical Research-Atmospheres*, *119*(14), 9041–9051. https://doi.org/10.1002/2014jd021578

Mahrt, F., Kilchhofer, K., Marcolli, C., Grönquist, P., David, R. O., Rösch, M., et al. (2020). The impact of cloud processing on the ice nucleation abilities of soot particles at cirrus temperatures. *Journal of Geophysical Research: Atmospheres*, *125*(3), e2019JD030922. https://doi.org/10.1029/2019JD030922

Mahrt, F., Marcolli, C., David, R. O., Grönquist, P., Barthazy Meier, E. J., Lohmann, U., & Kanji, Z. A. (2018). Ice nucleation abilities of soot particles determined with the Horizontal Ice Nucleation Chamber. *Atmospheric Chemistry and Physics*, *18*(18), 13363–13392. https://doi.org/10.5194/acp-18-13363-2018

Marcolli, C. (2014). Deposition nucleation viewed as homogeneous or immersion freezing in pores and Cavaties. *Atmospheric Chemistry and Physics*, *14*(4), 2071–2104. https://doi.org/10.5194/acp-14-2071-2014

Marcolli, C. (2020). Technical note: Fundamental aspects of ice nucleation via pore condensation and freezing including Laplace pressure and growth into macroscopic ice. *Atmospheric Chemistry and Physics*, *20*(5), 3209–3230. https://doi.org/10.5194/acp-20-3209-2020

Marcolli, C., Mahrt, F., & Kärcher, B. (2021). Soot PCF: Pore Condensation and Freezing framework for soot aggregates. *Atmospheric Chemistry and Physics*, *21*(10), 7791–7843. https://doi.org/10.5194/acp-21-7791-2021

Möhler, O., Benz, S., Saathoff, H., Schnaiter, M., Wagner, R., Schneider, J., et al. (2008). The effect of organic coating on the heterogeneous ice nucleation efficiency of mineral dust aerosols. *Environmental Research Letters*, *3*(2), 025007. https://doi.org/10.1088/1748-9326/3/2/025007

Murphy, D. M., & Koop, T. (2005). Review of the Vapour pressures of ice and supercooled water for atmospheric applications. *Quarterly Journal of the Royal Meteorological Society*, *131*(608), 1539–1565. https://doi.org/10.1256/qj.04.94

Murray, B. J., Wilson, T. W., Dobbie, S., Cui, Z., Al-Jumur, S. M. R. K., Möhler, O., et al. (2010). Heterogeneous nucleation of ice particles on glassy aerosols under cirrus conditions. *Nature Geoscience*, *3*(4), 233–237. https://doi.org/10.1038/ngeo817

Pach, E., & Verdaguer, A. (2019). Pores dominate ice nucleation on feldspars. *Journal of Physical Chemistry C*, *123*(34), 20998–21004. https://doi.org/10.1021/acs.jpcc.9b05845

Petters, S. S., Kreidenweis, S. M., Grieshop, A. P., Ziemann, P. J., & Petters, M. D. (2019). Temperature- and humidity-dependent phase states of secondary organic aerosols. *Geophysical Research Letters*, *46*(2), 1005–1013. https://doi.org/10.1029/2018GL080563

Piedehierro, A. A., Welti, A., Buchholz, A., Korhonen, K., Pullinen, I., Summanen, I., et al. (2021). Ice nucleation on surrogates of boreal forest SOA particles: Effect of water content and oxidative age. *Atmospheric Chemistry and Physics*, *21*(14), 11069–11078. https://doi.org/10.5194/acp-21-11069-2021

Reid, J. P., Bertram, A. K., Topping, D. O., Laskin, A., Martin, S. T., Petters, M. D., et al. (2018). The viscosity of atmospherically relevant organic particles. *Nature Communications*, *9*(1), 956. https://doi.org/10.1038/s41467-018-03027-z

Rissler, J., Messing, M. E., Malik, A. I., Nilsson, P. T., Nordin, E. Z., Bohgard, M., et al. (2013). Effective density characterization of soot agglomerates from various sources and comparison to aggregation theory. *Aerosol Science and Technology*, *47*(7), 792–805. https://doi.org/10.1080/02786826.2013.791381

Rogers, D. C. (1988). Development of a continuous flow thermal gradient diffusion chamber for ice nucleation studies. *Atmospheric Research*, *22*(2), 149–181. https://doi.org/10.1016/0169-8095(88)90005-1

Schiebel, T. (2017). *Ice nucleation activity of soil dust aerosols. (PhD)*. Karlsruhe Institute of Technology. https://doi.org/10.5445/IR/1000076327

Schill, G. P., De Haan, D. O., & Tolbert, M. A. (2014). Heterogeneous ice nucleation on simulated secondary organic aerosol. *Environmental Science and Technology*, *48*(3), 1675–1682. https://doi.org/10.1021/es4046428

Schnaiter, M., Büttner, S., Möhler, O., Skrotzki, J., Vragel, M., & Wagner, R. (2012). Influence of particle size and shape on the backscattering linear depolarisation ratio of small ice crystals – Cloud chamber measurements in the context of contrail and cirrus microphysics. *Atmospheric Chemistry and Physics*, *12*(21), 10465–10484. https://doi.org/10.5194/acp-12-10465-2012

Ullrich, R., Hoose, C., Möhler, O., Niemand, M., Wagner, R., Höhler, K., et al. (2017). A new ice nucleation active site parameterization for desert dust and soot. *Journal of the Atmospheric Sciences*, *74*(3), 699–717. https://doi.org/10.1175/JAS-D-16-0074.1

Umo, N. S., Wagner, R., Ullrich, R., Kiselev, A., Saathoff, H., Weidler, P. G., et al. (2019). Enhanced ice nucleation activity of coal fly ash aerosol particles initiated by ice-filled pores. *Atmospheric Chemistry and Physics*, *19*(13), 8783–8800. https://doi.org/10.5194/acp-19-8783-2019

Vali, G. (2008). Repeatability and randomness in heterogeneous freezing nucleation. *Atmospheric Chemistry and Physics*, *8*(16), 5017–5031. https://doi.org/10.5194/acp-8-5017-2008

Vali, G., DeMott, P. J., Möhler, O., & Whale, T. F. (2015). Technical note: A proposal for ice nucleation terminology. *Atmospheric Chemistry and Physics*, *15*(18), 10263–10270. https://doi.org/10.5194/acp-15-10263-2015

Vallon, M., Gao, L., Jiang, F., Krumm, B., Nadolny, J., Song, J., et al. (2022). LED-based solar simulator to study photochemistry over a wide temperature range in the large simulation chamber AIDA. *Atmospheric Measurement Techniques*, *15*(6), 1795–1810. https://doi.org/10.5194/amt-15-1795-2022

Virtanen, A., Joutsensaari, J., Koop, T., Kannosto, J., Yli-Pirila, P., Leskinen, J., et al. (2010). An amorphous solid state of biogenic secondary organic aerosol particles. *Nature*, *467*(7317), 824–827. https://doi.org/10.1038/nature09455

Wagner, R., Bertozzi, B., Höpfner, M., Höhler, K., Möhler, O., Saathoff, H., & Leisner, T. (2020). Solid ammonium nitrate aerosols as efficient ice nucleating particles at cirrus temperatures. *Journal of Geophysical Research-Atmospheres*, *125*(8), e2019JD032248. https://doi.org/10.1029/2019JD032248

Wagner, R., Höhler, K., Huang, W., Kiselev, A., Möhler, O., Mohr, C., et al. (2017). Heterogeneous ice nucleation of α-Pinene SOA particles before and after ice cloud processing. *Journal of Geophysical Research-Atmospheres*, *122*(9), 4924–4943. https://doi.org/10.1002/2016JD026401

Wagner, R., Hu, Y., Bogert, P., Höhler, K., Kiselev, A., Möhler, O., et al. (2024). Data sets for the research article "How Porosity Influences the Heterogeneous Ice Nucleation Ability of Secondary Organic Aerosol Particles" by Wagner et al. (2024) in the Journal of Geophysical Research (Atmospheres) [Dataset]. *Karlsruhe Institute of Technology*. https://doi.org/10.35097/e4xhczc6s8ebypv5

Wagner, R., Kiselev, A., Möhler, O., Saathoff, H., & Steinke, I. (2016). Pre-activation of ice-nucleating particles by the pore condensation and freezing mechanism. *Atmospheric Chemistry and Physics*, *16*(4), 2025–2042. https://doi.org/10.5194/acp-16-2025-2016

Wagner, R., Möhler, O., Saathoff, H., Schnaiter, M., Skrotzki, J., Leisner, T., et al. (2012). Ice cloud processing of ultra-viscous/glassy aerosol particles leads to enhanced ice nucleation ability. *Atmospheric Chemistry and Physics*, *12*(18), 8589–8610. https://doi.org/10.5194/acp-12-8589-2012

Wagner, R., Testa, B., Höpfner, M., Kiselev, A., Möhler, O., Saathoff, H., et al. (2021). High-resolution optical constants of crystalline ammonium nitrate for infrared remote sensing of the Asian Tropopause Aerosol Layer. *Atmospheric Measurement Techniques*, *14*(3), 1977–1991. https://doi.org/10.5194/amt-14-1977-2021

Wang, B. B., Knopf, D. A., China, S., Arey, B. W., Harder, T. H., Gilles, M. K., & Laskin, A. (2016). Direct observation of ice nucleation events on individual atmospheric particles. *Physical Chemistry Chemical Physics*, *18*(43), 29721–29731. https://doi.org/10.1039/c6cp05253c

Wang, B. B., Lambe, A. T., Massoli, P., Onasch, T. B., Davidovits, P., Worsnop, D. R., & Knopf, D. A. (2012). The deposition ice nucleation and immersion freezing potential of amorphous secondary organic aerosol: Pathways for ice and mixed-phase cloud formation. *Journal of Geophysical Research*, *117*(D16), D16209. https://doi.org/10.1029/2012jd018063

Wilson, T. W., Murray, B. J., Wagner, R., Möhler, O., Saathoff, H., Schnaiter, M., et al. (2012). Glassy aerosols with a range of compositions nucleate ice heterogeneously at cirrus temperature. *Atmospheric Chemistry and Physics*, *12*(18), 8611–8632. https://doi.org/10.5194/acp-12-8611-2012

Wolf, M. J., Zhang, Y., Zawadowicz, M. A., Goodell, M., Froyd, K., Freney, E., et al. (2020). A biogenic secondary organic aerosol source of cirrus ice nucleating particles. *Nature Communications*, *11*(1), 4834. https://doi.org/10.1038/s41467-020-18424-6